PHOTOIONIZATION OF GASES

IN THE EXTREME ULTRAVIOLET

MICHAEL JOSEPH HENNESSY , B.Sc. (HONS.)

Thesis submitted for the degree of
Master of Science
in
The University of Adelaide
(Department of Physics & Mathematical Physics)

October 1996

CONTENTS

ABSTRACT

The main goal of this thesis is the measurement of the total photoionization cross section of gases, principally Ar, O_2 and N_2, from approximately 200 to 600 Å, that is, in the Extreme Ultraviolet (EUV). The present aim is to reduce errors associated with the experimental acquisition of data and to achieve cross sectional results with total relative errors of less than ± 3%.

The emphasis of the experimental work was on the construction of a pulsed power supply capable of delivering peak currents of the order of a thousand amperes for use with a condensed spark discharge lamp, the design and implementation of an electrometer, built from discrete components, and a computer interface board.

Radiation from the lamp was dispersed by a grazing incidence monochromator before being passed into a double ionization chamber. The ion currents produced by the absorption of EUV radiation in the double ion chamber were grounded through their respective electrometers, whose readings used with other physical measurements, results in the total photoionization cross section being determined.

STATEMENT

This work contains no material which has been accepted for the award of any other degree or diploma in any university or other tertiary institution and, to the best of the my knowledge and belief, contains no material previously published or written by any other person, except where due reference has been made in the text.

I give consent to this copy of my thesis, when deposited in the University Library, being available for loan and photocopying.

SIGNED: .....**DATE:** 25/10/96

ACKNOWLEDGMENTS

To my supervisor, Dr. A. J. Blake, I wish to express my sincere gratitude for his limitless patience and easy accessibility whenever it was necessary to consult him for advice. I also thank Dr. D. G. McCoy for the many informative discussions on various experimental problems and, more importantly, their solutions. Also it would be remiss of me not to mention the technical staff for their extremely useful advice and hands–on help with many aspects of this work. Principally they were Messrs J. Wright and B. Nation, consecutive technicians with the UV Group, Messrs J. Smith and M. Shorthose from Electronic Services and Messrs P. Schebella, J. Schache and G. Eames from the department's Mechanical Workshop.

To my fellow students, especially those within my research group and in particular Messrs M. Panizza and A. L. Jones, I offer my gratitude for the time and assistance they freely gave. Also thanks to all fellow postgraduate students who offered a healthy social atmosphere outside the laboratory with various sporting activities and other not–so healthy social activities!

Lastly, but definitely not least, I thank Jennifer for her love, understanding and support above and beyond what can be reasonably expected. I truly hope that we both reap the rewards from what has been achieved here.

CHAPTER 1

Photoabsorption by gases

1.1 Introduction

The ultraviolet spectrum (~2 to 4000 Å) is divided into three parts with the extreme ultraviolet ("EUV") denoting wavelengths less than ~ 1000 Å. Solar EUV, which constitutes approximately 1% of the total solar flux, consists principally of emission lines that are totally absorbed by the earth's upper atmosphere. Solar EUV is partially responsible for the production of the ionosphere, a spherical shell of weakly ionized plasma extending from about 50 km to over 1000 km. Absorption occurs primarily by molecular nitrogen and oxygen coinciding with the E and F layers of the ionosphere, between approximately 50 and 150 km. The most intense emission line in the quiet solar spectrum below 600 Å, (the longest wavelength attainable here), is the 303.8 Å He II line, with the 256.3 Å He II and the 584.3 Å He I lines also being prominent. With increased solar activity, the solar flux in the short EUV can increase in intensity between 3 to 10. This, along with local factors, produces variations of the total ion concentration within the ionosphere which directly influences long distance radio communications and also results in ionospheric electrical currents which produces magnetic disturbances on the ground.

Exothermic reactions, with the vast majority involving ion–neutral interactions, pump energy into the ionosphere thereby driving the dynamic processes of the earth's upper atmosphere. Therefore, if the density profile for any of the major constituents is known, then using accurately measured laboratory total photoionization cross section (referred to as cross section from now on) values the ion production rates can be determined, providing us with the energy absorbed at any given altitude. Conversely, accurately measured laboratory cross sections used in conjunction with known absorption rates will provide improved density profiles. Actually the definitive model for the ionosphere can only be achieved with the inclusion of accurate energy distribution

functions for both primary and secondary photoelectrons as they are an important supplement of ionizing producing reactions. Accurate cross section measurements are also of immense importance in the fields of astrophysics, planetary sciences and radiation physics, chemistry and biology.

This work involves a study of the interaction of EUV with matter in a gaseous state, with the "first–order" process being photoabsorption. The term first–order alludes to interactions that are of the strongest form and are deduced from first–order perturbation theory. The most prominent photoabsorption process results from allowed electric–dipole transitions, with allowed electric–quadrupole and magnetic–dipole, both of which are second–order interactions, interaction rate magnitudes reduced by a factor of approximately 10^6. Interactions involving photoabsorptions include photoexcitation and photoionization, with the latter the most predominate in the EUV. Berkowitz (1979) provides a precis of second–order processes, however these are significant only at wavelengths outside the transmission range of the monochromator used here.

Previous researchers have measured cross sections with quoted accuracy's not better than 3% and with the majority closer to 10%. The aim here is to determine, with the greatest possible accuracy (< 3%), the cross sections of the major aeronomic gases at the most intense EUV solar emission line wavelengths. In order to achieve this, experimental difficulties, including the operation of sensitive instruments in the electrically noisy environment as a result of the nature of the light source used, must be overcome. It is anticipated that this can be achieved with shielding and optical coupling techniques on the data lines and the use of battery powered discrete component circuitry in instruments used for the detection and measurement of photoionization products.

1.2 Atomic absorption

Photoabsorption is the process whereby the absorption of a photon by an atom, result in the atom undergoing a transition to an excited state. Photoabsorption spectra, the simplest being that for a hydrogen–like atom, are divided into regions of discrete and

continuous absorption. The boundary between these regions corresponds to the ionization threshold. The discrete absorption is indicative that below the ionization threshold the atom can only exist in certain discrete energy states. The energy difference between the final and initial states is equal to the energy of the absorbed photon. The continuous absorption implies an infinite number of energy states. With the application of a voltage across the interaction region of the gas a current is extracted. This current attests to the formation of a free electron and positive ion with the electron stationary at infinity, that is with respect to the ion, for a photon energy equal to the ionization threshold. For a photon of energy greater than the ionization threshold the departing electron, to satisfy conservation of momentum, carries most of the surplus energy as kinetic energy, "ε", given by the Einstein relation, "$\varepsilon = h\nu - E_i$", where "$h\nu$" is the photon's energy and "E_i" is the ionization potential. This relation assumes that the ion is left in it's ground state. Figure (1-1) shown overleaf pictorially describes the energy levels of an atom and its corresponding absorption spectrum.

To fully appreciate this phenomenon and other process requires some knowledge of quantum mechanics.

1.3 Quantum mechanics

Quantum mechanics is a mathematical physical theory that provides a method for calculating quantities of atomic and molecular systems.

The foundation of quantum mechanics was the realisation by Planck and Einstein that electromagnetic radiation can in some circumstances be thought of as possessing particle–like properties. This enigmatic scenario was resolved by De Broglie with his fundamental theory of matter–wave duality, which is best expressed by the equation

$$\lambda = h / p \qquad (1.1)$$

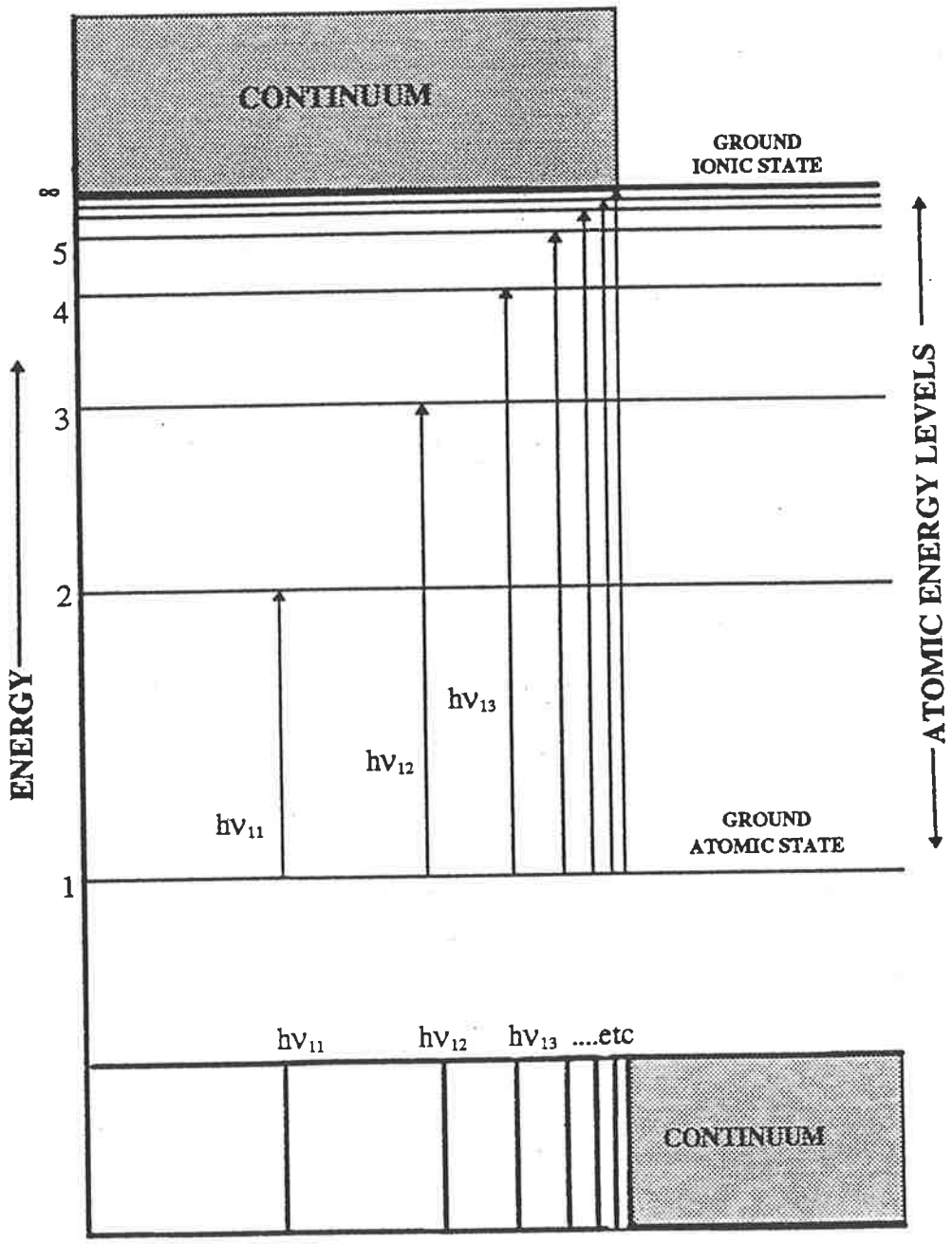

Figure (1-1). Schematic atomic energy level diagram with corresponding absorption spectrum line series.

and as h is very small the duality effect only manifests itself in the realm of atomic and subatomic particles. The above relation was later justified by electron diffraction experiments that produced interference patterns similar to those obtained with light. Another important aspect of quantum mechanics is the Heisenberg uncertainty principle, which states that any attempt of a physical measurement of a system results in a disturbance of the system with the consequence of limiting the precision of the measurement. The Heisenberg uncertainty principle is expressed as the canonically conjugate equations,

$$\Delta p \, \Delta x \geq \hbar$$
$$\Delta E \, \Delta t \geq \hbar \qquad (1.2)$$

and similar to De Broglie's matter–wave duality effect, the uncertainty principle is significant only on the scale of atomic and subatomic particles.

From the above it is evident that to adequately describe an atomic, and for that matter a molecular, system a suitable wave equation is necessary.

An atom consists of bound states of discrete energy called eigenvalues, "E_n", that are characterised by their matching wavefunctions (or eigenfunctions), "Ψ", which are solutions to the eigenvalue equation,

$$H \Psi = E_n \Psi \qquad (1.3)$$

The Hamiltonian operator, "H", is a differential operator for the total energy of the system, being equal to the sum of the kinetic and potential energies, and expressed in terms of the momentum and positional coordinates of the particle. For Ψ to be physically relevant it must be single valued, finite, and continuous everywhere, and with $|\Psi|^2 d\tau$ (where $|\Psi| = |\psi \, e^{\left(\frac{-i E t}{\hbar}\right)}| \equiv \psi^2$) defined as the spatial probability density distribution of the electron. For bound states, "$\psi \rightarrow 0$" exponentially with increasing distance from the

nucleus, thereby ensuring that the spatial probability density is localised about the nucleus. Eigenfunctions are peculiar to each bound electron and can be equally characterised by three "quantum numbers", "n", "l" and "m_l" which defines the electron's orbital, the orbital angular momentum and the component of the orbital angular momentum in the direction of an applied external magnetic field, respectively. A fourth quantum number, m_s, relates to the intrinsic spin of the electron where for multielectron atoms it interacts with the orbital angular momentum to produce multiplet splitting. Pauli's exclusion principle, another crucial axiom of quantum mechanics, requires that within the same system there can never be more than one electron in the same quantum state, that is no two electrons can possess four identical quantum numbers. This is borne out in the existence of chemically varying elements. In accordance with the exclusion principle two eigenfunctions from the same atomic system must be orthogonal to each other, that is

$$\int^{\infty} \psi_n \psi_m \, d\tau = 0 \quad \text{for } n \neq m \tag{1.4}$$

where n and m represent separate eigenstates originating from the same Hamiltonian. This is essentially in accordance with the Bohr picture of the atom with the electrons contained within well defined orbitals.

The Hamiltonian for the multielectron atom is

$$H = V_{eff.}(r) - \frac{\hbar^2}{2\,m} \Sigma_j \, \nabla_j^2 \tag{1.5}$$

where $V_{eff.}(r)$, is the net Coulomb potential experienced by an electron due to the nucleus and the electrostatic force from the remaining j–1 electrons. The quantum mechanical Hamiltonian is obtained with the substitution of the energy operator,

$$E = i\,\hbar \frac{\partial}{\partial\, t} \tag{1.6}$$

to produce the time–dependent Schrödinger Equation, ("S.E."),

$$i\,\hbar\frac{\partial\,\Psi(r,t)}{\partial\,t} \;=\; -\;\frac{\hbar^2}{2\,m}\nabla^2\,\Psi(r,t) \;+\; V(r,t)\,\Psi(r,t) \qquad (1.7)$$

which is the required form for solving time varying interactions such as photoabsorption (see footnote [1] below). The eigenfunctions are then given by an expansion in terms of the stationary states, $\Psi_n = \Sigma_n\, a_n(t)\, \psi_n(r)\, e^{\left(\frac{-i\,E\,t}{\hbar}\right)}$, of the initial unperturbed system. The energy operator from above, the momentum operator and the linear operator, are all hermitian operators, and with Ψ known, they can be utilised to calculate expectation values, within the limitations set by the Heisenberg uncertainty principle. For example the expectation value for the radius of the electron's orbit, which is comparable to the Bohr radius, is given by,

$$r_{av.} = \int^{\infty} \Psi^*(r,t)\; r\; \Psi(r,t)\; dV \qquad (1.8)$$

where "Ψ^*" is the complex conjugate of Ψ. The expectation value or the average of a real observable quantity can be found using it's corresponding operator.

The potential $V_{eff}(r)$ is non–central, and this ensures an inability to solve the S.E. directly, however Hartree (1928) partially overcame this problem. He firstly assumed that each electron in a multielectron system can be described by its own independent wave function. Then the total spatial wavefunction can be separated into the product of all the j single electron wavefunctions,

$$\Psi_T = \Psi_1\Psi_2\Psi_3.....\Psi_j \qquad (1.9)$$

[1] The Schrödinger equation has undoubtedly been successful in predicting experimental results, however no conformation for the electron to be described by a wave function, which is the foundation for wave and quantum mechanics, has until recently been elicited. Lohmann and Weigold (1981) using noncoplanar symmetric (e, 2e) techniques have measured the velocity (momentum) distribution functions for electrons in atomic hydrogen which they found to be in agreement with the momentum profile given by the absolute square of the probability amplitude obtained from the solution of Schröedinger's equation for the ground state of hydrogen.

where each electron "sees" a spherically symmetric field formed by the sum of the attractive nuclear spherical field and the approximated spherically repulsive field provided by the other $j-1$ electrons (the central field approximation). This composite potential is used to numerically solve the S.E. and the calculated eigenfunctions used to determine a new potential. This new potential is used to generate new improved eigenfunctions that leads to a further refinement of the potential. This procedure is repeated until a potential is self–consistent to a high order of accuracy, that is until there exists a negligible difference between two successive potential functions. Hartree's method however does not allow for the indistinguishability of any two electrons and for spin–orbit effects. Fock (1930) included the former in his method by using antisymmetric total eigenfunctions for the electrons (the stronger form of the exclusion principle). Spin-orbit effects arise from the vectorial sum involving all the electron's orbital and angular momenta, and not that of an individual electron, being quantised. Herzberg (1950) simplified proceedings by noting that for closed shells, that is when the orbital contains the maximum number of electrons, the vectorial sum of the orbital and angular momenta will be zero and therefore make no contribution to the sum. Hartree–Fock results compare favourably with experimental observations are similar to those calculated from Hartree's method, the exception being for excited states of atoms.

Absorption of radiation can be studied using time dependent perturbation theory, by assuming a weak interaction between the radiation and the atom, the absorption intensity can be readily derived from a semi–classical treatment, such as carried out by Marr (1968), to produce

$$I_{i\to f} = \frac{2\pi^2}{3h^2\varepsilon_0}\rho(\nu)\left|\int \psi_f^* \, \mathbf{er} \, \psi_i \, d\tau\right|^2 \qquad (1.10)$$

where $I_{i\to f}$ is the probability of transition from the initial state, i, to the final state, f, ε_0 is the permittivity of free space, $\rho(\nu)$ is the radiation density at a given frequency, ν, and **er** is the electric dipole moment of an electron. The integrand is the dipole approximation

of the sum of the squared matrix elements for the transition. The energy of the absorbed radiation must naturally be equivalent to the energy difference between the final and initial state energies.

Transitions between all states are required to adhere to symmetry and conservation laws, otherwise known as selection rules, which are applied to determine allowable transitions. Below is a list of selection rules for photoabsorption involving allowed electric–dipole transitions for multielectron–atoms

$$\Delta S = 0$$

$$\Delta L = \pm 1$$

$$\Delta J = 0, \pm 1$$

where S and L are the total spin and orbital angular momentum respectively, and J, (= S + L), the total angular momentum.

1.4 Atomic photoionization

An expression for the photoionization cross section of a bound system can be deduced from quantum electrodynamics or time dependent perturbation theory. From quantum electrodynamics and following Herzberg's (1950) notation the intensity for the absorption of radiation can be expressed by

$$I_{abs.}^{nm} \sim \upsilon_{nm} \left| R^{nm} \right|^2 \qquad (1.11)$$

where ν_{nm} is the frequency of the absorbed radiation corresponding to the transition from the lower n to the upper m state, and R^{nm} is the electric dipole matrix element which is defined as

$$R^{nm} = \int \psi_f^* \, \Sigma_j \, e^{(ik\,r_j)} \nabla_j \, \psi_i \, d\tau \qquad (1.12)$$

where $\mathbf{r_j}$ is the position of the jth electron and $\mathbf{k}$ the propagation vector of the radiation. The probability of a transition between two states, ψ_i and ψ_f, is proportional to the square of it's matrix element. The exponential term in the above integrand can be expanded to give

$$e^{i\mathbf{k}\cdot\mathbf{r_j}} = 1 + i\mathbf{k}\cdot\mathbf{r_j} - \frac{(\mathbf{k}\cdot\mathbf{r_j})^2}{2!} - \ldots\ldots\ldots \qquad (1.13)$$

For wavelengths greater than the dimensions of the atomic or molecular system, as is the case for EUV radiation, the above exponential reduces to $e^{i\mathbf{k}\cdot\mathbf{r_j}} \approx 1$. This is known as the dipole approximation as it is used to evaluate the dipole moment $\mathbf{er}$.

The photoionization cross section, which has dimensions of area, is related to the intensity and therefore the probability of the photoionizing event occurring at a given wavelength for a given orbital. The total photoionization cross section is the sum of the partial cross sections for each orbital multiplied by its order of degeneracy, that is the number of electrons in that orbital. The principle difficulty in calculating the photoionization cross section is in accurately describing the ionized electron's wavefunction. Two different approaches consider the state of the nuclear electric field through which the ionized electron moves has been previously theorised. Common to both approaches is that the one electron wavefunction can be separated into the product of the radial and angular wavefunctions, where the angular wavefunction is assumed to remain unchanged after the transition and so the integral in equation (1.2) reduces to an overlap of radial wavefunctions. Cooper's (1962) unrelaxed core approximation is that of the j single electron wavefunctions from the initial state, j–1 remain unchanged after the ionization transition. Further, the ionized electron is considered to experience the same effective central field both before and after ionization takes place. The integral then reduces to the overlap of the radial wavefunctions of the one electron before and after ionization. The relaxed core approximation (Seaton (1951)) is that the final state wavefunction is formed by the antisymmetricalized product of the free electron and the one–electron wavefunction

of the ionic core. The ionized electron is then treated as moving in the effective central field of the residual ion with allowance made for electron exchange. The relaxed core model considers no effect, apart from exchange effects, of the outgoing electron on the ionic field while the unrelaxed core model overestimates this effect. The unrelaxed ionic core approximation is preferred for ionization from an inner shell, while for ionization involving a valence electron, as is the case here, the relaxed core approximation is suitable. Cooper noted that the best effective central field, for consideration of photoionization calculations, is neither the field of the relaxed ion or the unrelaxed ionic core, but one between these two extremes. The integral in equation (1.2) reduces to the product of an integral over one electron wavefunctions of the form of Cooper's unrelaxed core approximation and an overlap integral which describes the relaxation of the ionic core. The continuum wave function can be chosen from

(1) plane waves

(2) Coulomb scattered waves for $Z_{eff.}$

(3) waves calculated from Hartree's $V_{eff.}(r)$

(4) waves calculated from Hartree-Fock's $V_{eff.}(r)$

with the accuracy of the results increasing down the list. With the exception of (1), for which $V(r) = 0$, they are all based on models assuming a spherically symmetrical potential. For Coulomb type functions, the photoelectron is scattered by the average charge distribution of the ion, which gives a reasonable degree of accuracy at low interaction energies. However, plane waves, that have been Schmidt orthogonalised, are also satisfactory for highly energetic photoelectrons where the interaction between the ion and photoelectron is negligible

Photoionization doesn't necessarily involve valance electrons and for non–hydric atoms there exists quasi–discrete states whose total energy is greater than that corresponding to the first ionization threshold. These states arise from either two–electron or inner–electron excitations. These discrete states can couple with an underlying

electronic continua, assuming a sufficient mixing of the wavefunctions, to effect ionization (autoionization). Simultaneous two-electron excitation is prominent when configuration interaction or correlation effects are important. Physically the autoionization process occurs when the excitation energy of the ionic core is greater than the binding energy of the electron. Then, with no other competing decay paths available, autoionization results from a close encounter between the ionic core and the electron. This enables transference of the core's excitation energy to the electron so that the electron can overcome it's binding energy and therefore escape the ionic field.

The only examples for which the photoionization cross section has been successfully calculated to match the experimental data are those of helium and atomic hydrogen, where analytic expressions for the bound and unbound wavefunctions have been accurately determined.

The dipole selection rule requires that the angular momentum quantum number must differ by unity after photoionization, so there are two possible final states (except for an initial state with $l = 0$). However, Bethe and Salpeter (1957) showed that the transition probabilities and hence the transition intensities generally obey the condition; $I(l+1) >> I(l-1)$. The calculation of the cross section is then simplified with only the one overlap integral contributing to the total cross section.

(Cooper, 1962) determined that the spectral shape of the cross sections of some elements can be understood by considering the energy dependence of the overlap integral. Figure (1-2) is of a plot of outershell radial wavefunctions and d–plane waves for $\varepsilon = 0$, that is for zero photoelectron energy, for Ne, Ar and Kr. As the photoelectron energy increases, the d waves wavelengths will shorten and appear to move towards the origin. For Ne the overlap between the wavefunctions will increase and correspondingly the cross section will also increase. However for Ar and Kr the wavefunction's overlap and hence the cross sections will decrease with increasing photoelectron energy, becoming zero when the positive and negative portions of the integral completely overlap. The cross section, when plotted as a function of the wavelength, will therefore contain a dip that is known as

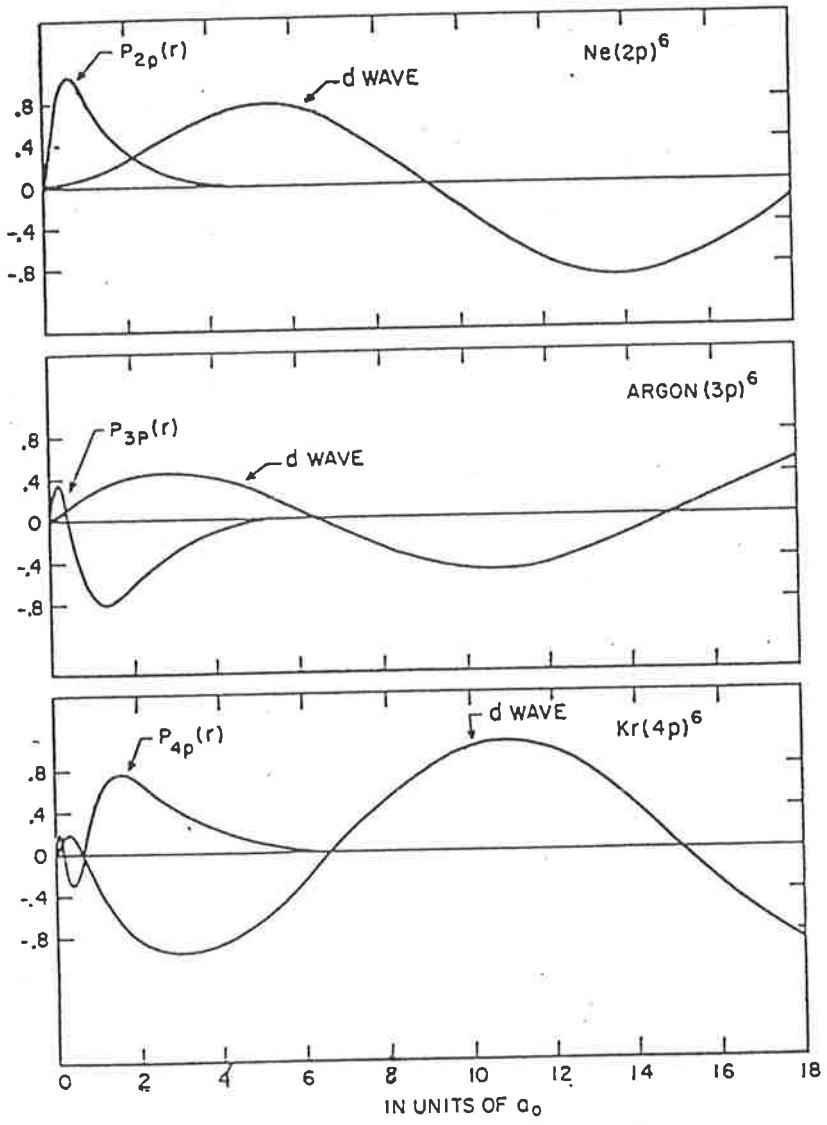

Figure (1-2). Outer subshell radial wavefunctions and d waves for $\varepsilon = 0$ for Ne, Ar and Kr. (From Cooper(1962)).

the Cooper minimum. Cooper also proposed that ground state cross sections from atomic subshells whose radial wavefunctions are nodeless don't generally display a Cooper minimum, where the number of nodes is equated to n–*l*–1. For Ar there exists a node in the wavefunction for the 3p valance orbital which results in the dramatic dip of the cross section at ~250 Å.

Finally there is a dependence on the cross section upon the type of orbital from which the electron is ejected for orbitals whose potential contains a centrifugal barrier (known as shape resonance). The net effective potential, for the 4d→f transitions, for a central field, can be expressed as the summation of the Coulombic attraction and the centrifugal repulsion terms. The potential curves for such orbitals comprises a deep inner well, a small repulsive barrier and finally a broad well. The inner well is the result of the strong attraction of the only partially screened full nuclear charge on the electron. At larger distances from the nucleus screening of the nuclear charge becomes more effective and the repulsive centrifugal term dominates over the weakened nuclear attraction term. The centrifugal term remains constant for a series of atoms for a given *l*, but the degree of screening varies as one proceeds from a compact electron distribution to a more diffuse distribution. At still greater distances from the nucleus the longer range 1/r attractive potential overcomes the $1/r^2$ repulsive centrifugal term to form a broad well. Centrifugal effects associated with 4d→f transitions, with 4d→p transitions having a low intensity, have been known to have a dramatic influence on their cross section spectra. For the rare earth elements, a potential barrier of 10–20 eV restrains low energy f orbits outside the 4d orbital region. Therefore, only at energies great enough for the f–electron's wavefunction to penetrate inside the barrier is there a sufficient mixing of the states wavefunctions. Put another way, the escaping electron must receive enough energy to overcome the barrier for the 4d→f transition to occur. This effect is most pronounced for the rare earth elements where a delayed onset of ionization from the 4d subshell reaches a maximum approximately 30 eV above threshold. Whilst this effect occurs in the soft x-ray spectral range, this effect is important for small non–hydric diatomic molecules.

The observance of the Cooper minimum is not confined to atomic systems, and can be expanded to include molecular systems especially when dealing with atomic orbitals within the molecule.

1.5 Diatomic molecular absorption

Diatomic molecules are formed when atomic valence electron orbitals envelope both atoms to produce molecular orbitals. The molecular orbital mathematically expressed in the Hartree–Fock approximation has provided the theoretical platform for some accurate calculations of a wide variety of molecular phenomena. The approximate shape of molecular orbitals can be obtained by treating molecular orbitals to be constructed by a combination of atomic orbitals belonging to the constituent atoms, the linear combination of atomic orbitals (LCAO) approximation. The molecular orbitals then can be simply divided into several classes. Core orbitals describe the inner electron orbitals and are therefore well represented by atomic orbitals. Valance orbitals describe the molecular shape and may extent over the full volume of the molecule. The molecular orbitals are occupied in accordance with the Pauli exclusion principle.

Molecular photoabsorption is far more complex than for atoms, as can be visualised by examining their spectra with the appearance of many diffuse bands. This complexity is a result of the extra degrees of freedom for molecules, that is rotation and vibration between the nuclei. The molecule then has electronic, vibrational and rotational energies compounding to give the total energy of the molecular state. Studies of the fine structure of rotational bands clearly indicates that simultaneous rotation and vibration occurs. In fact the rotational levels contribute no observable effect with the present work and can therefore be ignored. Of the many series of bands in a molecular spectrum, occasionally they can be fitted to a Rydberg series that converges to an ionization threshold. Typically, however, these bands are associated with vibrational progressions that converge onto a dissociation limit, resulting in the disintegration of the molecule into its constituent atoms. Berkowitz (1979) however noted that applying the assumption that

the transitional rates for ionization and dissociation are based upon the relative speeds of the electron ($> 10^7$ cm s^{-1}) and the nuclear vibration ($\approx 10^5$ cm s^{-1}), ionization would always dominate EUV absorption. The above processes can, however, be readily discerned with the identification of the ionic products using a mass spectrometer.

The potential curve for a molecule is that of an anharmonic oscillator and is usually represented by the Morse function (see figure (1-3)). Each electronic state is characterised by its potential curve, which has an infinite number of vibration levels converging to it's dissociation energy for the molecule. Only when the potential curve displays a minimum can the molecule be said to exist in a stable electronic state.

Molecular spectra, despite its apparent complexity, provides a vast amount of information that can be quantitatively retrieved by applying the Born–Oppenheimer, or the adiabatic, approximation. This approximation, due to the relatively slow motion of the nuclei with respect to the electron, enables the molecular wavefunction to be separated into the product of the electronic and nuclear wavefunctions (which can be further reduced to the vibrational wavefunction), i.e.

$$\psi_T = \psi_e . \psi_v \qquad (1.15)$$

The intensity of a transition from one state to another can be calculated by the Franck–Condon principle, which states that the electronic transitions occur so fast that the internuclear distance remains relatively unchanged during a transition (the sudden approximation). The wave mechanical treatment of the Franck–Condon principle assumes a small dependence on the electronic wavefunction by the internuclear distance, and so the electronic transition moment can be approximated by a constant to yield the following expression,

$$I_{i \to f} \propto \left| \overline{R}_e \int \psi'_v \psi''_v d\, r_v \right|^2 \qquad (1.16)$$

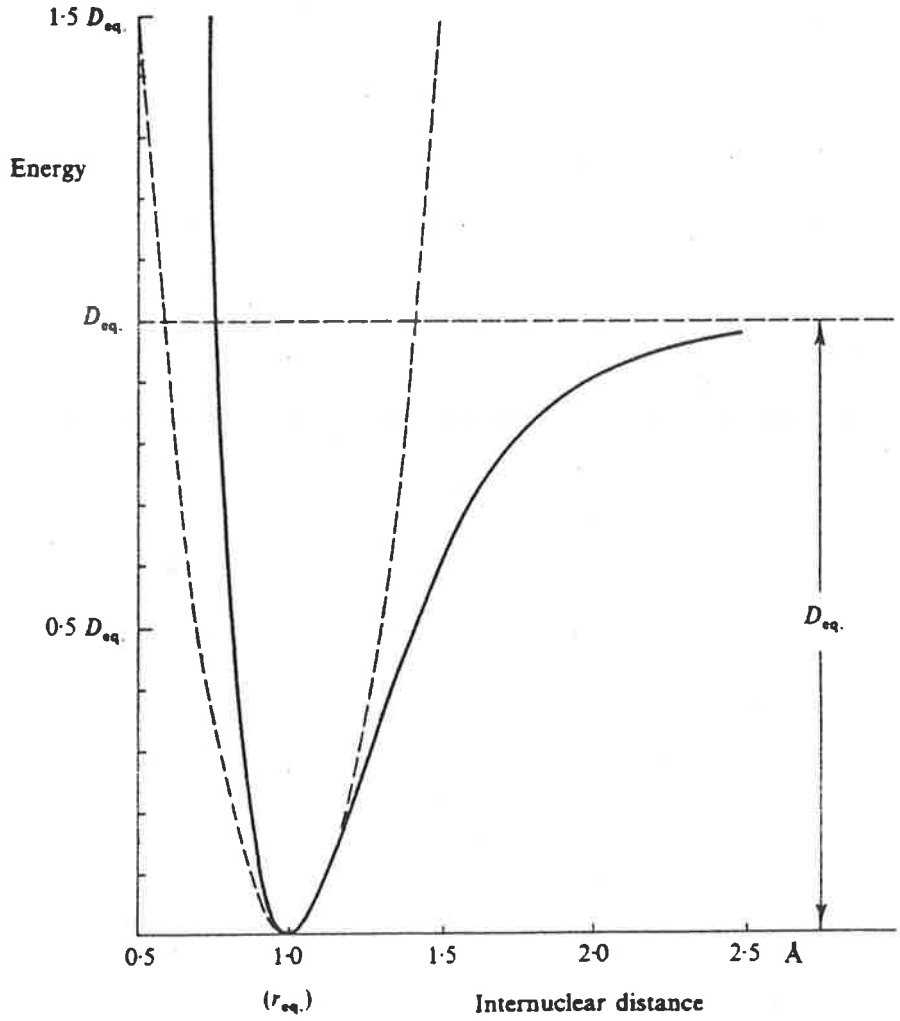

Figure (1-3). Schematic diagram of a Morse function for a typical diatomic molecule (solid line), together with the ideal simple harmonic parabola (Banwell (1972)).

where R_e is the electronic transition moment. The transitional probability, and hence the intensity, is proportional to the square of the integrated product of the initial and final vibrational wavefunctions (the so called overlap integral). The Boltzmann distribution at room temperature ensures that the vast majority of molecules are found in the vibrational ground state, v_0, and so the most intense transitions will involve those for which the final vibrational state has a maximum vertically above that for the initial state, as shown in figure (1-4).

For photoionization the minimum photon energy required to remove the least bound electron will result in a transition to the ground molecular ion state. Some electronic states for O_2 are shown in figure (1-5), where the ground and first ionic ground states are depicted along with some unbound states. Increasing the energy to the interaction will result in the kinetic energy of the ejected electron increasing until the second least bound electron's ionization limit is reached with this process competing with the former process. Total photoionization cross section measurement experiments do not discriminate between the final ionic states, the possible ionized dissociation products, or the ionization process (such as preionization). Preionization, which is analogous to the atomic autoionization process, occurs when an inner shell electron is excited to a discrete state that exists within a continuum state that corresponds to the formation of an ion and a free electron. Predissociation is a process that is analogous to preionization, except that the continuum state corresponds with the disintegration of the molecule into it's constituent atoms. The result is a radiationless transition to the relevant continuum state.

As for atomic transitions, there also exist selection rules for molecular transitions. However the lack of a spherically symmetrical net potential in molecules necessitates the use of the component of the electronic orbital angular momentum, for linear molecules, along the internuclear axis, "Λ", to define a "good" quantum number. For Λ values of 0, 1, 2,... the respective states symbols are Σ, Π, Δ,... with the quantum number "Σ" defined as the component of the total electron spin, "S", along the internuclear axis. A further labelling of the states symbol refers to the symmetry of the electron's wavefunction with

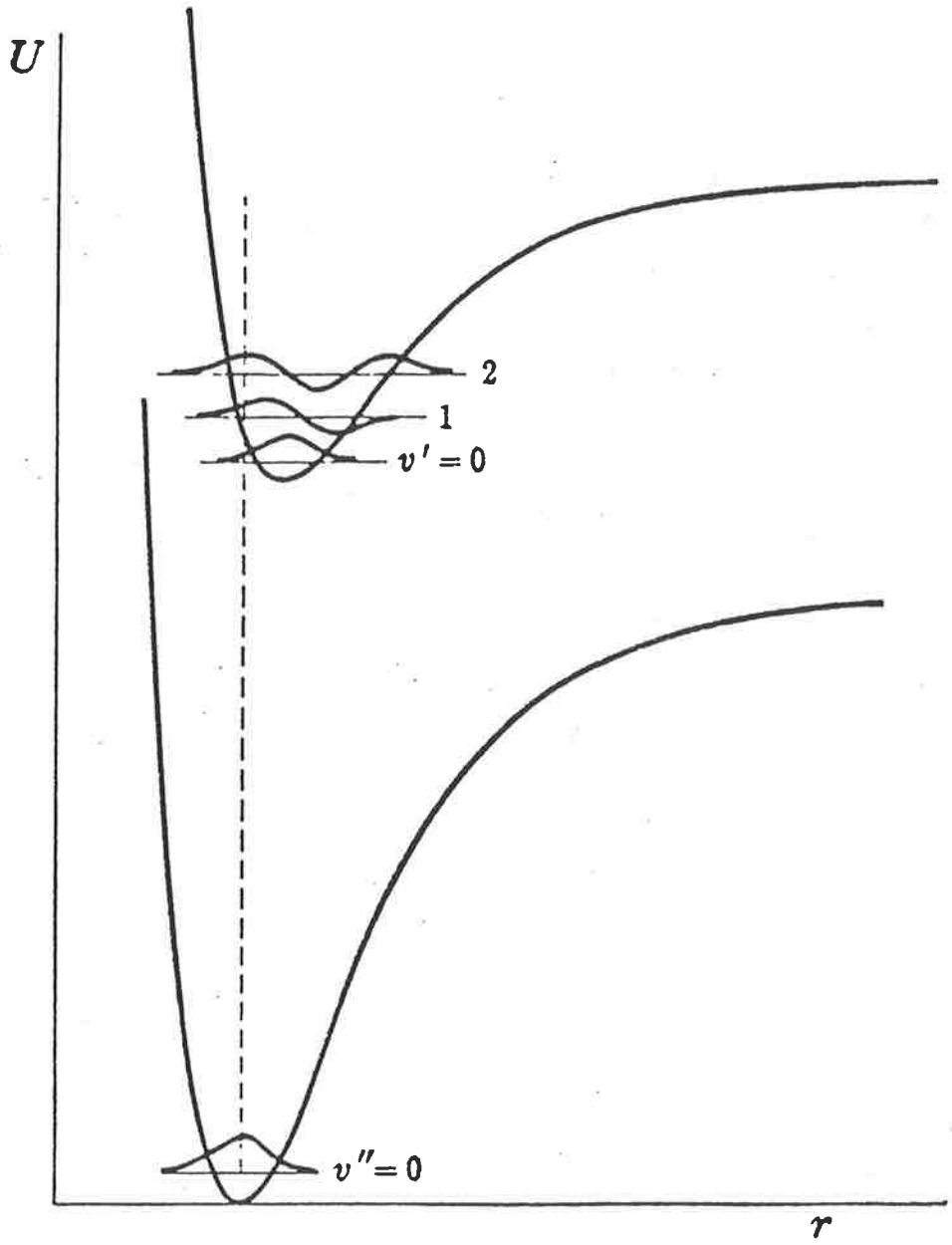

Figure (1-4). Franck-Condon intensity schematic diagram showing that the greatest overlap of the eigenfunctions occurs between the ground state and with the second vibrational level of the upper excited state, shown as the vertical dashed line (Herzberg (1950)).

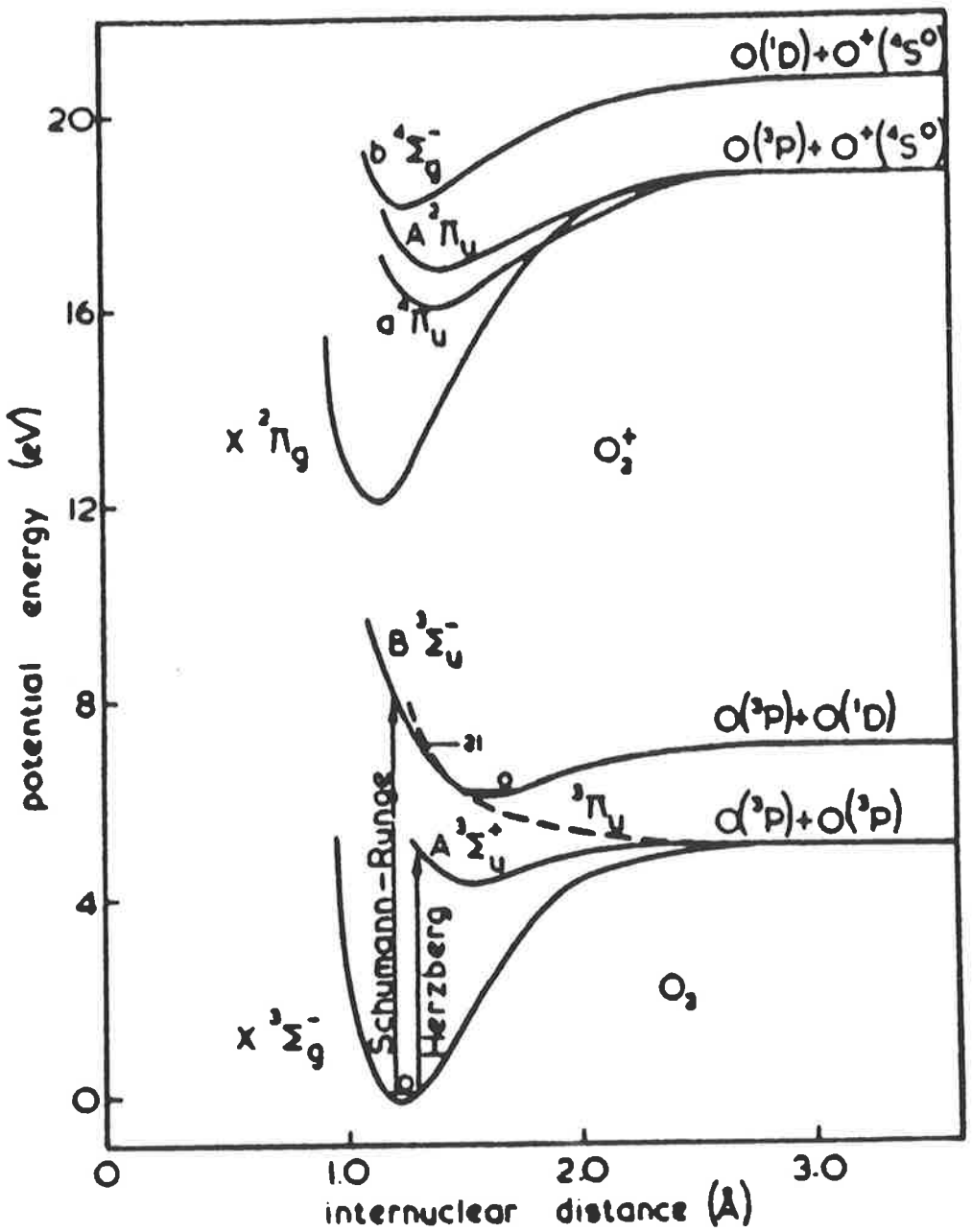

Figure (1-5). Major electronic states of molecular oxygen, all of them bound states except for the dissociating $^3\Pi_u$ state.(Marr (1967)).

respect to the plane containing both nuclei. A "+" and a "–" superscript indicates, respectively, an unchanged and a changed wavefunction respectively after a reflection in the plane. Symmetry selection rules are also applicable for reflection through the plane containing both nuclei, with like terms interchanging only with like terms (eg. $\Sigma^{+} \rightarrow \Sigma^{-}$). For homonuclear molecules the orbitals or the wavefunctions have definite parity about the midpoint of the internuclear axis, and are designated as "g" if even and "u" if odd, with a change in the parity after a transition, for example g↔u). The multiplicity of a molecular state is identical as for atoms, that is 2S + 1, and is indicated as an upper prefix of the state's symbol.

Where the initial and final electronic states are $^{1}\Sigma$ singlet states, that is where the total electronic angular momentum, ($\Omega = \Lambda + \Sigma$), about the internuclear axis is zero, then the angular momentum of nuclear rotation is identical to the total angular momentum, "J". Then the selection rule is equivalent to that of a simple rotator,

$$\Delta \Lambda = 0, \pm 1 \quad \text{except } \Lambda = 0 \not\rightarrow \Lambda = 0 \tag{1.17}$$

There are selection rules that are generally adhered to for an allowed electric–dipole transition, with those regarding like terms, and for homonuclear nuclear molecules, symmetry terms, already mentioned above. These additional selection rules are,

$$\Delta J = 0, \pm 1 \quad \text{except } J = 0 \not\rightarrow J = 0$$
$$\Delta S = 0 \tag{1.18}$$

For all other transitions the various coupling modes of the angular momenta have to be determined, so as to decide which quantum numbers are "good" for defining the correct selection rules. Hund's coupling cases provides such a guide. However deviations from these cases are not too infrequent because of an inability to correctly ascertain the magnitude of the interactions within the molecule. This is particularly true for interactions

involving states with a high degree of rotation where the angular momentum vectors are uncoupled from the internuclear axis. Hund's case (a) assumes that the interaction between the nuclear rotation and the electronic motion is very weak but the electronic motion is coupled very strongly to the internuclear axis. Then the total angular momentum, "J", is defined as the sum of Ω with the angular momentum of the nuclear rotation, "N", as is the case for the symmetric top. In Hund's case (b) the electronic spin momentum is weakly coupled to the internuclear axis. The non–zero Λ and N are summed to give the total angular momentum without the spin, "K" which then couples with S to form J.

For both states belonging to case (a) the quantum numbers Σ, Ω and J are well defined and the selection rules are,

$$\Delta \Sigma = 0$$
$$\Delta \Omega = 0, \pm 1$$
$$\Delta J = 0 \text{ for } \Omega = 0 \rightarrow \Omega = 0 \qquad (1.19)$$

For both states belong to case (b) the quantum number K is well defined and the selection rules are,

$$\Delta K = 0, \pm 1 \text{ with } \Delta K \neq 0 \text{ for } \Lambda = 0 \rightarrow \Lambda = 0 \qquad (1.20)$$

The work here is concerned mainly with major aeronomic gases so I will now discuss briefly their term symbols for the ground and ionized ground states. The ground state for N_2 is denoted by $X^1\Sigma_g^+$ where X denotes the molecular ground state. The valence electron is a $3\sigma_g$ orbital electron and the ionized ground state is given by $X^2\Sigma_g^-$. For O_2 the ground state is $X^3\Sigma_g^-$ and with the valence electron a $1\pi_g$ or $1\pi_g^*$ orbital electron and the ionized ground state is accordingly $X^2\Pi_g$. Ionized states of higher energy are given a precursor of A, B, C, etc for increasingly higher states with the same multiplicity.

1.6 Molecular photoionization

When examining aspects of molecular photoionization, as is the general case of molecular photoabsorption, problems arise with the anisotropy of the multicenter molecular field and the interaction among (ro–) vibrational modes. Improvements in this field has been gained through the development of realistic, independent–electron models and the adaptation of multichannel quantum defect theory to molecular photoionization.

As analogous with atoms, dynamic structure in molecular cross section curves occur. However, structure in the cross section is often masked because of other progenitor electron orbitals exist whose energy levels may differ by only a few eV from the electron orbital.

The cross sections for N_2 and O_2 both display bumps or shoulders near 200 Å and were first theoretically investigated by Cohen and Fano (1966). They discussed the effect in terms of Huygen's approach and noted that each molecular atom should behave as an independent absorber of light with the resultant scattered photoelectron waves from each molecular atom producing interference effects. Compounded with this effect is the atomic selection rule $\Delta l = \pm 1$ is invalid for molecules and Δl can take any odd value for homonuclear molecules (to satisfy parity conservation). Transitions to states with high l are unlikely as the electron is prevented form the region of the ground state by centrifugal force. Then the transition probability will increase with successively higher l final state waves for increasing photon energy. This is identical to the shape resonance model discussed in the atomic photoionization section. Shape resonance effects appear to be prominent among small, non–hydride molecules and with $l = 3$ this effect becomes prominent with a photon energy in the range of approximately 30–60 eV. The above was showed to be valid with the shoulders in the cross sections for N_2 and O_2, at approximately 280 and 330 Å respectively, coinciding with the maxima in the partial cross sections for the $3\sigma_g \rightarrow$f transitions (see figure (1-6)).

Dehmer et al (1969) have theoretically predicted that shape resonances represent an important class of exceptions to the Franck–Condon vibrational intensity distributions

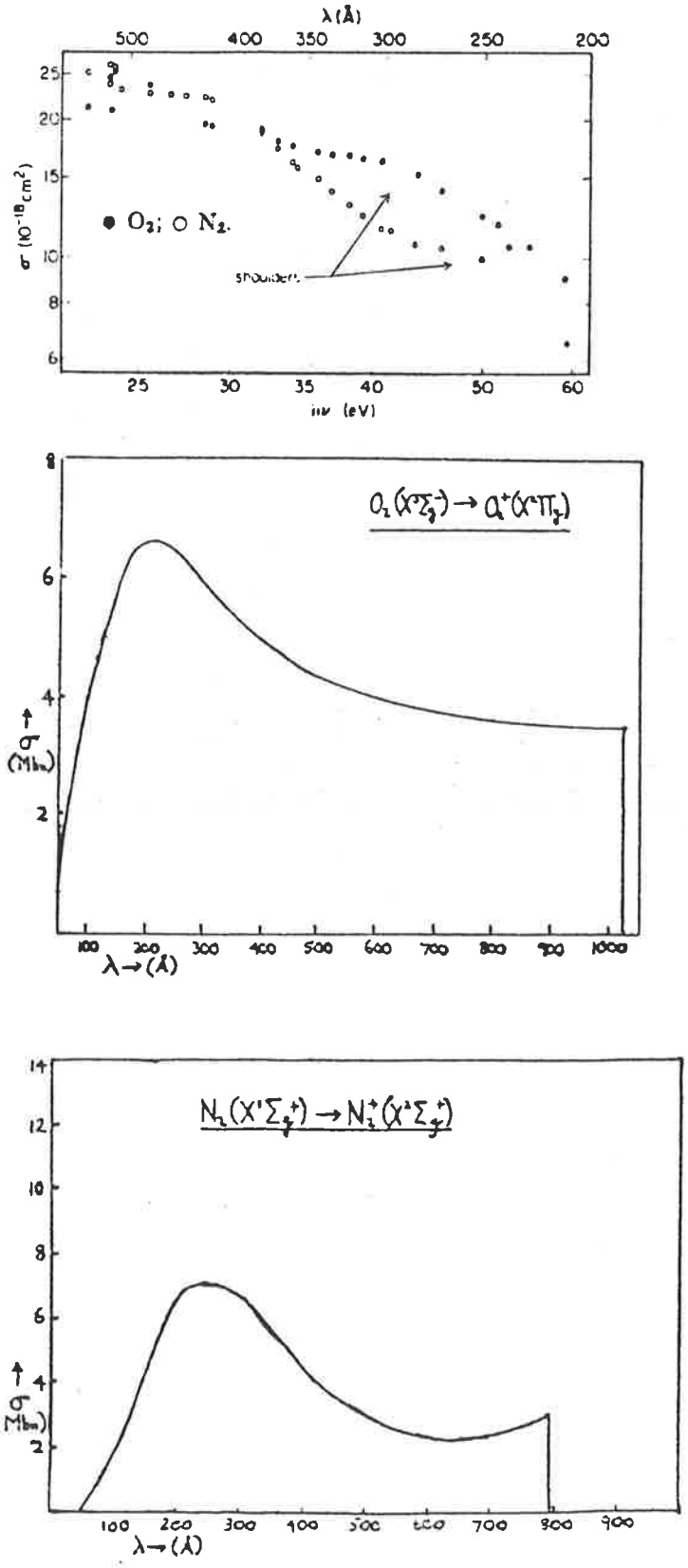

Figure (1-6). Top diagram (a) is a logarithmic plot of the experimental photoabsorption cross sections for molecular oxygen and nitrogen, showing the shoulders (Cohen and Fano (1966). The bottom diagrams (b) is of the cross sections for $1\pi g$ (or $1\pi g^*$) and $3\sigma g$ bound orbitals for oxygen and nitrogen respectively (Tuckwell 1969).

within the final ionic state for regions free from preionization, predissociation or ionization thresholds. They directed their investigations to the $3\sigma_g \rightarrow \varepsilon\sigma_u$, $\varepsilon\pi_u$ photoionization channel of $N_2X^1\Sigma^+_g$. The breakdown of the FC principle stems from the nature of the shape resonance effect. The potential barrier and the corresponding energy and lifetime (width) of the resonance are sensitive functions of the internuclear distance (R). Then the above will vary significantly over the range of R corresponding to the ground state vibrational motion. They found the time delay of the photoionization event, that is associated with the spectral shape resonance effect, enhances the coupling between the nuclear motion and the electronic motion, invalidating the FC factorisation of the two modes. Also the effects are larger for vibrational intensities, and angular distributions, and where significant they exist over large wavelength regions, $\approx$ 100 Å.

CHAPTER 2

Light production

2.1 EUV Light Sources

Light sources for the EUV are divided into continuous and discrete line emission sources. The principle advantage of the continuous light source is its complete coverage of the region of the spectrum under investigation, and assuming that the dispersion instrument's resolution is high enough and the lamp's spectra is smooth, then any fine structure in the absorption spectrum can be accurately studied. The only continuum sources of sufficient intensity to cover the EUV region are synchrotrons, storage rings, and free electron lasers (FEL). The existence of overlapping higher–orders, which was for many years a serious problem with the first two sources, can be easily negated with the use of modern filters, or predispersion grating methods. The cost of such sources are, however, prohibitively high and so are beyond the budget of most research institutions. However, precise measurements of photoionization cross sections can be obtained using discrete line emission sources.

Discrete emission lines can be easily produced by passing an electrical discharge through an ionizable gas or vapour. The radiation emitted from the source is usually dependent upon the gas filling, the voltage employed to produce the discharge, the current through the lamp, and other operational conditions of the lamp (see below). To appreciate the mechanism of these light sources it is necessary to review the basic processes for the generation of radiation that is produced by the passage of a current through an ionizable gas, that is a gas discharge. Following this a precis of discharge characteristics, that are considered relevant to this work, including breakdown criteria and the internal structure of discharges will be presented.

2.2 Gas discharge theory

2.2.1 Introduction

Gas discharges are classified into two distinct classes, self–sustaining and nonself–sustaining. A self–sustained discharge requires no external aid for the initiation and for the continuation of the discharge. For the nonself–sustaining discharge however, an external influence is mandatory for the discharge to start and be maintained. An external influence could be an incandescent cathode or an UV illuminated cathode, both of which supply a constant source of electrons to the discharge. The following will only deal with self–sustained discharges, the class of discharge employed for the present work.

2.2.1a Gas discharge light production

Excitations, including ionizations, result from suitably energetic electrons impacting with gas atoms, or molecules. The spectrum of the line radiation is dependent upon the electron temperature, or the energy distribution, and the gas density.

With a low electron temperature the line radiation is in the infrared, however with a sufficiently high electron temperature the atoms will be raised to more energetic states and thus emit lines of shorter wavelengths. For an electron temperature of approximately 10 eV the majority of the atoms will be singularly ionized with multiply–ionized atoms being also possible. The reduction of the screening of the nuclear charge in multiply–ionized atoms leads to a greater energy difference between the bound states so that the line radiation is emitted mainly at shorter wavelengths in the VUV and X-ray regions of the spectrum.

The radiation emitted during the passage of an electrical current through an ionizable gas at low pressure, $\leq$ 10 Torr, is due to radiative electron recombination. Milne (1924) statistically determined that the probability of electron capture with the emission of radiation varies inversely to the free electron temperature at small ion speeds. Low capture cross sectional values correspond to a high electron energy, with the perturbation by the

electron on the gas atom decreasing as the interaction time period decreases. Excitation rates due to neutral or excited atomic impacts are comparable to electron impacts only when the neutral or excited atoms have attained double the required excitation energy which is intrinsically improbable at low gas pressures. The frequency of radiative recombination at low pressures is negligible compared to the more highly probable process of excitation via electron collision because the number of excited states is negligibly small compared with the number of ground state atoms, $\sim 10^{-10}$:1. Additionally recombination of ions and electrons occurs principally via a non–radiative process at the walls of the discharge tube. This accounts for the well known fact that EUV gas discharge sources are of low intensity.

2.2.2 Breakdown mechanisms

Initially I will consider breakdown criteria as they apply to dc discharges, since they are not only the simplest but their mechanism is indicative for all types of discharges.

For sufficiently low voltages applied between two electrodes separated by a gap, containing a gas, the gas is an insulator. However as the voltage is increased to the breakdown voltage, V_B , the gas spontaneously becomes conductive. This sudden transition marks the occurrence of a spark. The spark has been defined by Loeb (1939) as "an unstable and discontinuous occurrence marking the transition from one more or less stable condition of current between electrodes in a gas to another one". The outcome of this spark is critically dependent upon the voltage across the electrodes, the discharge current, the gas and pressure of the gas. Figure (2-1) overleaf is a schematic diagram of the voltage–current characteristics of dc gas discharges. When the current in the discharge is increased from A, as shown in figure (2–1), the potential between the electrodes remains constant until B, where space charge effects begin to have an influence on the discharge characteristics, and the potential between the electrodes drops rapidly. The region C–D is a transitional region and is usually subdivided into the corona and the sub–normal glow discharge.

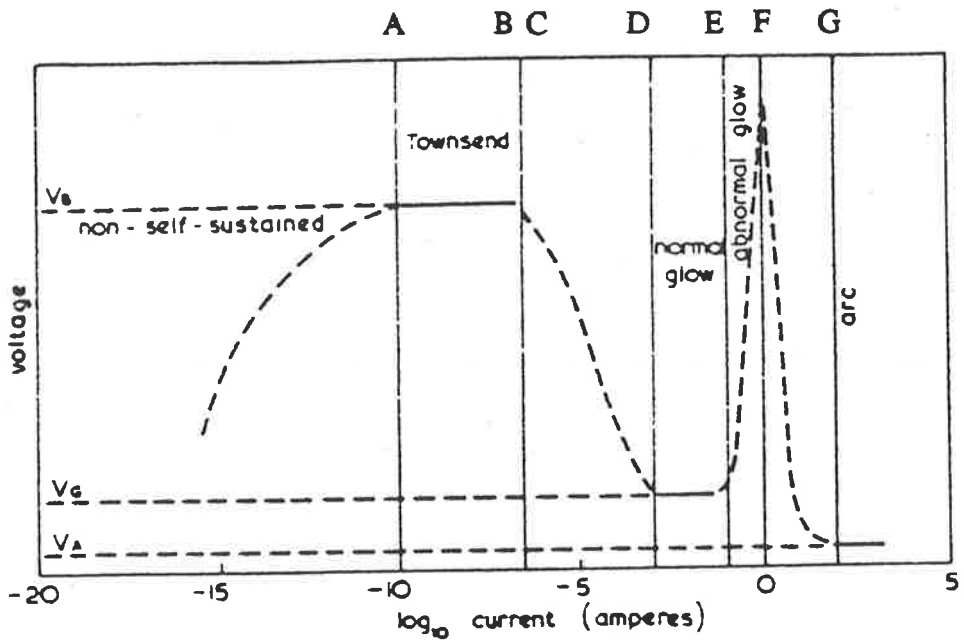

Figure (2-1). Voltage-current characteristics of a low pressure discharge with the stable regions that can be self-sustained labelled:
V_B the breakdown voltage, V_G the normal glow discharge, and V_A the arc discharge (Marr (1967)).

The Townsend discharge is characterised by currents of the order of 10^{-12} to 10^{-6} amperes, and the electrical resistance of the gas is typically in the range of megaohms.

The breakdown voltage is itself insufficient to cause ionization of the gas, therefore the primary electron in the gap is produced by natural radioactivity or cosmic rays. The electron is then accelerated towards the anode until it has gained enough energy to ionize a gas atom with the resultant electrons being accelerated by the field until they can further ionize gas atoms. The process repeats itself, thereby producing an avalanche of electrons sweeping towards the anode. Because of the low mass of the electron compared to the ion, the electron avalanche will sweep across the gap with the ions left relatively motionless. This mechanism was investigated by Townsend (1910) who showed that the final electronic current, i, was related to the initial electronic current, i_0, by the following expression

$$i = i_0 e^{(\alpha d)} \qquad (2.1)$$

where α, the Townsend primary ionization coefficient, is the number of ionizing collisions per unit length of path and d is the gap distance. Equation (2.1) is applicable for small distances or low voltages only, and with an increase of the gap distance or the voltage, the current increases at a rate greater than given by equation (2.1). Townsend correctly surmised that secondary electrons were being produced and equation (2.1) was easily modified to accommodate this secondary process, giving

$$i = \frac{i_0 e^{(\alpha d)}}{1 - \gamma \left[e^{(\alpha d)} - 1\right]} \qquad (2.2)$$

where γ, Townsend's second ionization coefficient, is the sum of all ionization coefficients that result in the formation of secondary electrons. These secondary electrons are mainly created by positive ions impacting with the cathode, and to a lesser extent, photons from the discharge ionizing gas atoms and/or the

photoeffect at the cathode. From equation (2.2) it can be deduced that the boundary between a self–sustaining and nonself–sustaining discharge is $\gamma\,[e^{(\alpha\, d)} - 1] = 1$ or, since $\gamma << 1$ is true for the majority of gases,

$$\gamma\, e^{(\alpha\, d)} = 1 \qquad (2.3)$$

This condition defines the spark breakdown criterion, and the onset of a discharge. This implies that the breakdown can occur as a result of a single primary electron, with an associated avalanche and it's accompanying secondary processes being sufficient to regenerate the primary electron at the cathode. The discharge is then said to be self–sustaining. Assuming that an ion impact at the cathode is the most important mechanism of the secondary processes, the formative time lag or the breakdown time is inversely proportional to the ion drift velocity, that is in the microsecond range (F. Llewellyn Jones, (1966)). Since all the above processes are statistical, the cumulative effects of a number of avalanches are needed to ensure the discharge will continue. For $\gamma\, e^{(\alpha\, d)} < 1$ the discharge is nonself–sustaining, while the growth of the discharge current increases more rapidly with $\gamma\, e^{(\alpha\, d)}$ increasing above unity.

The breakdown criteria has been expressed by Nasser (1971) as

$$p\,d = \frac{1}{f(V_B\ /\ p\,d)} \ln\left[1 + \frac{1}{\phi(V_B\ /\ p\,d)}\right] \qquad (2.4)$$

where $f(V_B / p\,d)$ and $\phi(V_B / p\,d)$ are functions of α / p and γ / p respectively and with the assumption that α / p and γ / p are functions of E / p, where "E" is the electric field strength across the gap and "p", the gas pressure. This had been experimentally verified and was extensively studied by Paschen (1889). Equation (2.4) can be succinctly expressed as

$$V_B = F\,(p\,d) \qquad (2.5)$$

The breakdown voltage of a uniform gap is then given by a unique function of the product of the pressure and the gap distance for a given gas and electrode material. The above relationship is known as the Paschen's Law. Physically, p d , is a measure of the number of mean free path lengths across the gap. Deviations from Paschen's Law are particularly common for the extreme values of p d. Consideration of equations (2.4) and (2.5) reveals that V_B is also a function of E / p. Nasser (1971) derived a mathematical relation between V_B and p d as ,

$$V_B = \frac{B\,p\,d}{\ln\left(\frac{A\,p\,d}{\ln\left(1+\frac{1}{\gamma}\right)}\right)} \qquad (2.5)$$

where B and A are constants intrinsic to the gas and dependent upon the gas temperature. Examination of the above relation for large values of p d shows V_B to be quasi–linear with p d, as in agreement with experiments. However, for smaller values of p d, the denominator initially tends to zero faster than the numerator, hence a graph depicting V_B plotted as a function of p d contains a minimum, the Paschen minimum, $V_{b_{min}}$. Figure (2-2) illustrates a typical Paschen curve for a gas contained between planar electrodes. With the voltage across the planar electrodes less than $V_{B_{min}}$ it is impossible to achieve breakdown across the gap irrespective of the gap distance or gas pressure. A number of experimental investigations to confirm Paschen's Law have been conducted, eg. Carr (1903) and Llewellyn Jones and Henderson (1939), all in agreement with equation (2.5) for values of p d $\leq$ 200 mmHgcm. However, for p d >200 mmHgcm, the Townsend mechanism must be replaced by a "streamer" mechanism to explain the experimental observation of a significantly reduced formative time lag.

The streamer theory for breakdown was independently proposed by Raether (1939), Loeb (1939) and Meek (1940). The streamer theories differ on the specific

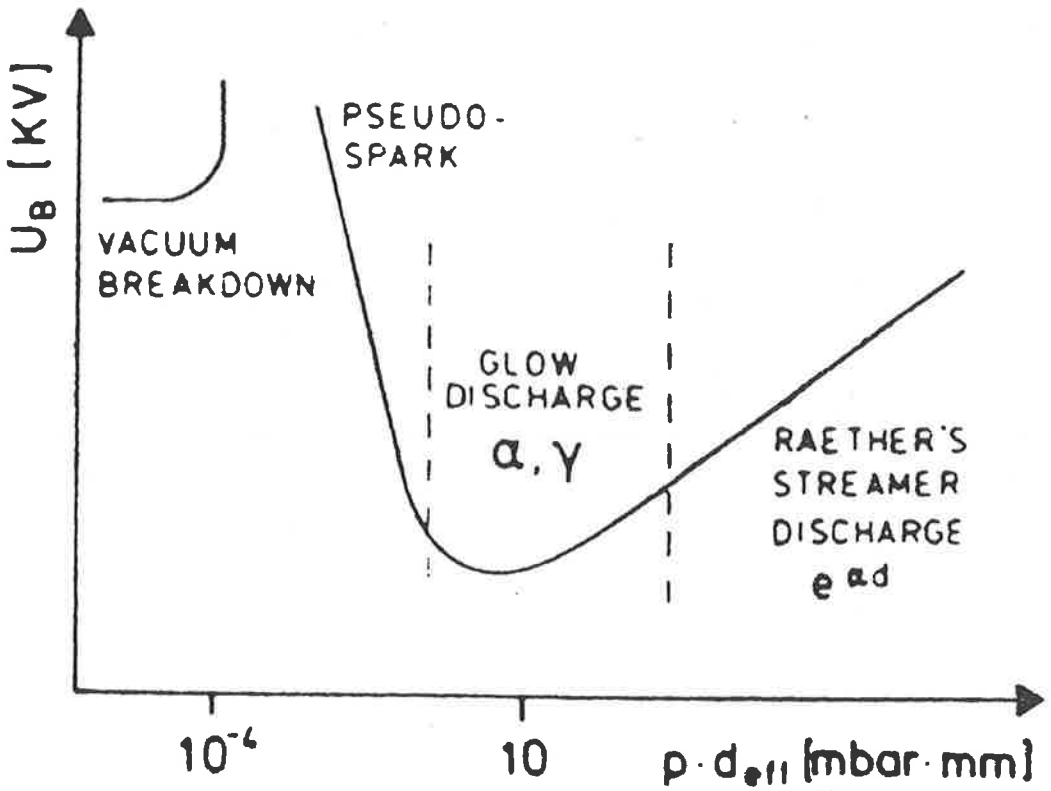

Figure (2-2). Typical Paschen curve (Bloess et al (1983)).

mechanism for the streamer formation, however common to all is the integral role of photoionization in the generation of new streamers a distance from the initial streamer. Meek and Craggs (1953) summarised the streamer mechanism by firstly assuming that the initial avalanche had successfully bridged the gap with the avalanche electrons being swept up by the anode. Secondary electron avalanches are then formed in the gas surrounding the cone–shaped positive ion column by photoionization from photons emitted by the densely ionized plasma in the head of the column. When the radial field strength about positive space charge at the head of an positive column attains that of the externally applied field strength, the secondary electron avalanches will be drawn into the column. This leads to an augmentation of the column space charge towards the cathode. The rapid growth of the positive space charge across the gap constitutes a streamer and breakdown of the gap occurs when the streamer reachers the cathode. This creates a highly ionized plasma channel resulting in a spark crossing the gap. With a greater applied voltage across the gap, the initial electron avalanche can form mid–gap and the growth of the positive space charge across the gap is achieved via secondary electron avalanches from both in front and behind the positive column. The development of a streamer, or a leader stroke, followed by return stroke is exactly what is observed, by using high speed cameras, during lightning strikes.

Supplemental research has been extensive into the intricacies of the development of the streamer or spark discharge, with those relevant to this work discussed here. Fisher and Bederson (1951) experimentally investigated the dependence of the formative time lag with p d. They found that for low overvoltaged gaps, that is applied voltages slightly above V_B, long formative time lags were evident for p d values up to 1000 mmHg cm. Increasing the overvoltage leads to a decrease in the formative time lag. They attributed this to an increasingly greater positive space charge, with a resultant increased field strength, and to the photoelectric effect at the cathode. The fact that the overvoltage magnitude, and not p d, was the principle factor determining the formative time lag was later confirmed by computer analysis by Ward (1965). Allen and Phillip (1964) expanded

on Fisher and Bederson's experiment with a greater range of voltages and for a number of gases. Their results also showed that the formative time lag is a function of the percent overvoltage, and furthermore that a deviation in the associated voltage curve versus formative time lag was an indication of the transition from the Townsend to streamer regime.

Summarising the findings by the above and other researchers, the Townsend avalanche mechanism with the modifications including space charge and photoelectric effects can adequately describe the breakdown process overvoltages < 20 %. For ≥ 20 % overvoltages and large p d values, the streamer theory predominates. At still greater overvoltages ($\approx 200 - 300$ %), Starnevich and Kalinin (1968) observed a broad channel as opposed to a filamentary channel. Babich and Stankevich (1973) theorised that this can be explained by proposing that runaway electrons are being produced in the gap by these high fields which was experimentally verified by Tarasova et al (1974). Mesyats et al (1972) observed formative time lags that were not in agreement with those predicted by the streamer model for overvoltages between those quoted above. They noted that the formative time lag was also dependent upon the number of electrons at the cathode. For a small number of initial electrons, which Mesyats et al took to be one, the formative time lag was longer than that proposed by the streamer model. They found that the avalanche stopped growing due to a decrease in the field strength at the avalanche head as photoionization played no role in the breakdown mechanism. At this point a new avalanche develops ahead of the parent avalanche with the same cycle repeated. Mesyats et al called this the avalanche chain model, where a chain of avalanches joined "head to toe" traverses the gap.

Kunhardt and Byszewski (1980) model unified all post–Townsend breakdown mechanisms. This model was based on the existence of two components in the energy distribution function of electrons; that is slow (thermal) and fast electrons. Because the effective retarding force on an electron diminishes with increasing electron speed, the fast electrons escape ahead of the avalanche. Once ahead of the avalanche they enter a region

with a decreased field strength and become trapped where losses due to ionization equal the energy gained from the depleted field. The "trapping" distance is dependent upon the initial energy of these electrons. These "seed" electrons are continuously ejected from the avalanche and create new avalanches at a distance ahead of the parent avalanche. The photoelectric effect at the cathode also produces secondary electrons that are subsequently accelerated towards the high field region of the parent avalanche head. The electron energy distribution function has still to be experimentally determined and therefore at present no model can be conclusively validated until such a distribution can be obtained.

2.2.3 Glow discharge

The lamp used here was operated in both a dc and pulsed mode for the generation of EUV radiation. The external electrical circuit parameters ensured that the "V–I" characteristics of the lamp were such that a glow discharge was achieved in the dc mode. Townsend and spark discharges can be described as operating by a pulse mechanism (Mason, (1978)), whereas the glow discharge is a pulseless phenomenon although the ignition of the glow is via a spark, with the average current through the discharge determined by any external resistance. Pulsed glow discharges that are often referred to in publications are in fact abnormal glow discharges because the current density emitted per unit area from the cathode surface is too large to be strictly termed a glow discharge (Mason (1978)).

Figure (2-3) portrays the typical internal structure of the glow discharge. Not all of the defined regions pictured in figure (2-3(a)) are crucial to the discharge, and a displacement of the anode to A_1, results in the discharge remaining virtually unchanged, though the positive column will be absent. This is in contrast with the movement of the anode left of A_1, with the quenching of the discharge as the anode passes M. This demonstrates that the discharge processes nearest to the cathode are crucial to the mechanism of the discharge.

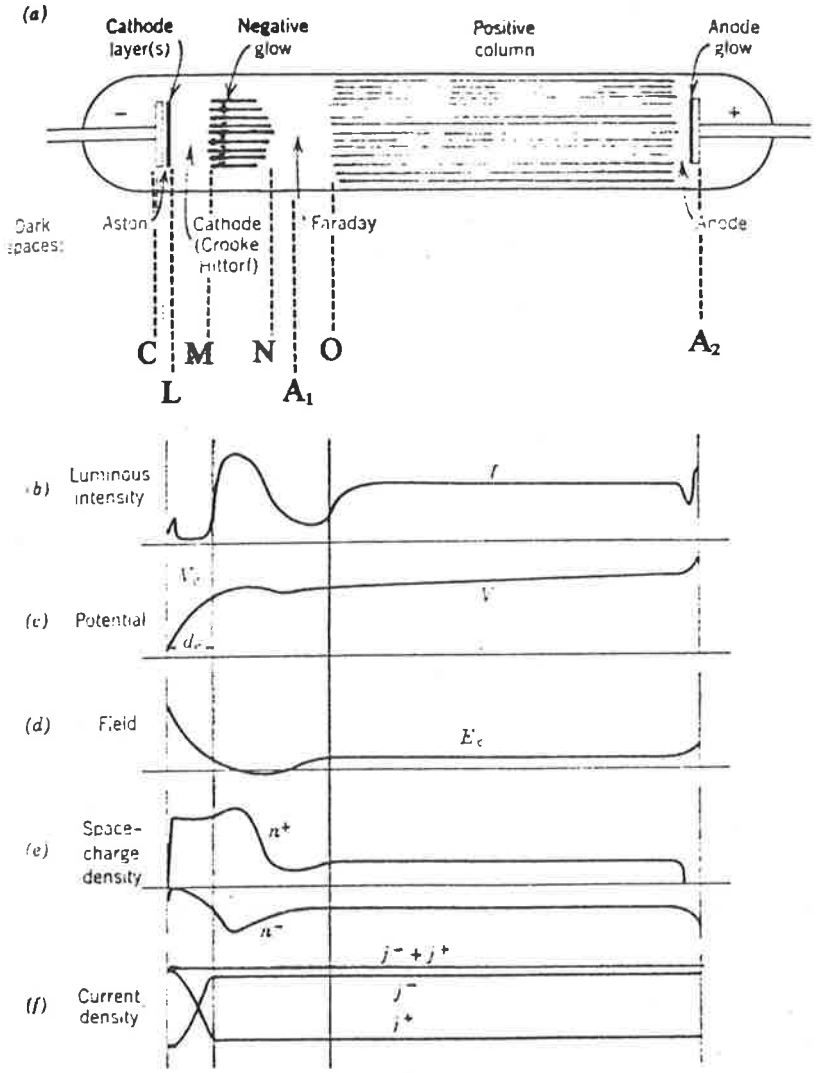

Figure (2-3). The normal glow discharge internal structure for neon in a 50 cm tube at 1 torr pressure between the cathode C and the anode for two different positions, A_1 and A_2. Diagram (*a*) shows the optical phenomena with the luminous intensity being indicated by the density of the hatching and also diagrammatically shown in (*b*). Diagram (*c*) is the potential along the tube that is generated by the presence of space charges where the majority of the voltage drop occurs between the cathode and the leading edge of the negative glow. This potential profile results in an axial field with a high field existing naturally near the cathode. Diagram (*e*) is of the distribution of space charges along the tube where the preponderance of a positive space charge in the negative glow results in the glow results in the rapid rise of the potential as seen in (*c*). Lastly (f) shows the current densities where the high positive-ion current in only the cathode region can be gleaned from (*e*), whereas the electron current is greater throughout the other regions (Nasser (1971)).

The various regions of the glow discharge have been reported in great detail by many authors, therefore I will expand in some detail only the region that is pertinent to the lamp used, the negative glow.

2.2.3a Negative glow

The negative glow is the most luminous region of the glow discharge, see figure (2–3(b)), with the maximum intensity near the negative glow's leading edge. This maximum in the light intensity is a result of the inelastic collisions by electrons that have been accelerated to high energies by the cathode fall, thereby inducing excitations of the gas atoms. Further inelastic interactions by the already energy depleted electrons result in the glow becoming less luminous until it merges into the Faraday dark space. Comparisons of mono–energetic electron beam ranges as a function of electron energy correspond with experimentally determined negative glow lengths showing that excitations occur by electron collisions.

With the minimum current required for the normal glow the cathode dark region and the cathode area containing the glow discharge occupies a small fraction of the lamp's volume and cathode respectively. The current can be increased by over two orders of magnitude while the voltage across the discharge remains constant. This is achieved by the glow discharge expanding over the cathode surface proportionally with the current, shown as D to E in figure (2-1), so the cathode current density remains constant. The discharge spot on the cathode is prevented from expanding, to cover the whole surface of the cathode over almost the entire normal glow discharge current range. Analysis shows that, except at the discharge core axis and at the boundary of the discharge tube, there exists a negative potential difference between the core of the discharge and a transverse point outside the core, resulting in a sinusoidal radial component of the electric field, "E_r". This radial field accelerates the positive ions outwards and is an equivalent effect to ion self–repulsion. For a given current and voltage, a virtual increase of the discharge column radius reduces E_r causing the column to contract. Conversely, a reduction of the discharge

radius results in the widening of the discharge spot at the cathode. As the discharge current is increased, the greater ion current accelerated out of the discharge column increases E_r leading to an increase in the discharge column radius. When the whole cathode surface is covered by the discharge an increase of the discharge current can only be achieved with an increase in the cathode fall, E to F in figure (2-1). With a further increase of the current the cathode is heated until the majority of secondary electrons are produced by thermionic emission with a drop in the cathode fall, and marked with the formation of an arc discharge. Because of their low number densities, (except at the Faraday dark space/negative glow boundary), electrons do not have an appreciable effect on the local field.

2.2.4 Hollow cathode effect

When a planar cathode is replaced with a cylindrical hollow cathode ("H.C."), discharge currents up to three magnitudes greater with the same operational conditions are realised. This has been known for a considerable time with the first hollow cathode glow discharge reported by Paschen (1916). However the mechanism of the discharge has only recently been satisfactorily explained.

A further advantage of the H.C. over the planar cathode is that the discharge generates a much higher current density at a lower cathode fall for the identical operational conditions thereby reducing the amount of sputtered material from the cathode. The latter is due to the H.C. operating in the glow discharge mode, as opposed to an arc where thermionic emission causes heating of the cathode. In any case Anders et al (1993) showed that sputtered ions interact with an intense electric field, (see below), immediately upon leaving the cathode and return uneventfully to the cathode. Neutrals typically have a mean free path for interactions that is much greater than the H.C. diameter. As will be shown below the emission lines of the H.C. also possess a small line width due to the low electric field strength existing in the negative glow region and a low gas temperature.

The H.C. effect can be best understood by studying the glow discharge produced between two parallel cathodes and a planar anode orientated perpendicular to, and some distance from the cathodes. As the distance between the cathodes is reduced the discharge current, at a critical stage, increases exponentially. This dramatic increase occurs when the two separate negative glows begin to coalesce. Gewartowski and Watson (1965) reported that the H.C. discharge will only operate within a limited range for p D, where p is the gas pressure and D the hollow cathode diameter, which they determined for the rare gases is 1 mmHg·cm $\leq$ p D $\geq$ 10 mmHg·cm. Also the H.C. radius must be greater than the cathode fall distance d_c , and as d_c is inversely proportional to the pressure, (Cobine (1958)), this condition will determine the lower limit of the pressure at a given applied voltage for the H.C. effect.

Ngo et al (1990) investigations of the H.C. concluded that initially the discharge exists in a low current discharge mode and at a critical pressure switches to a high current mode where the current increases by more than three orders of magnitude. Their temporal studies showed that the low current discharge mode exists for several hundredths to a few microseconds when the discharge is initiated above the transitional pressure. This transitional pressure was determined to be inversely proportional to the H.C. diameter (Yu et al (1982)). This ties in with Cobine's (1958) finding that d_c is inversely proportional to the pressure.

Studies of the transition mechanism during the low to high current phase has shed a great deal of light upon the H.C. effect. When the central plasma column is fully developed, the anode equipotential lines move toward the cathode during the transitional phase and so that the potential on the discharge axis at the H. C.'s orifice approaches the anode potential (Pak and Kushner (1989)). Some 100 ns. later, the cathode–anode voltage drop collapses almost completely to a thin sheath adjacent to and mirroring the cathode surface . Therefore, an extremely high field is formed within a few tens to hundreds of microns above the cathode surface and a second breakdown from the centre of the negative glow to the H.C. surface develops. Von Engel (1983) suggested this could be due to

electrons oscillating between the H.C. walls and the negative glow (the "pendulum effect"). Ngo et al (1990) applied an axial magnetic field to the H.C. so that electrons were prevented from oscillating and instead were forced to move transversely to the electric field, with the resultant effect that the discharge did not develop beyond the initial low current discharge mode. This strongly suggests that the pendulum effect is responsible for the high current mode.

2.2.5 Low pressure spark discharge

The basic mechanism of the low pressure spark discharge has already been covered in section 2.2.2 so I will limit my discussion in this section to the experimental studies of the temporal characteristics of such discharges. I will initially discuss the development of a low pressure spark discharge for low overvoltage gaps and follow this with the case for high overvoltage gaps.

Rogowski and Tamm (1928) observed that for discharges that progress from the Townsend to a spark discharge, there existed three distinct stages in the collapse of the voltage across the gap. They identified the first stage corresponded with a diffuse glow discharge and the final stage being the formation of a concentrated discharge channel along which the spark traverses. The duration of the intermediate stage, a concentrated glow discharge, which they measured to be less than 1 μs for discharges passed through air at 185 mT, increases rapidly with decreasing pressure. Doran (1968) photographed the transformations of a diffuse to a concentrated glow discharge phase, with the latter showing a typical glow structure, to a filamentary discharge channel. The transition from a glow to a spark discharge occurs only with the formation of cathode spots, which precedes the formation of the concentrated glow discharge, and are associated with a rapid rise in the current (Kekez et al (1970)).

The existence of the diffuse glow phase is critically dependent upon the size and shape of the electrodes. With very large plane electrodes the diffuse glow phase, although transitory and typically less than 1 μs, is quite prominent while with pointed electrodes it

usually is absent. The diffuse glow structure consists of a bright luminous region (cathode fall) in front of the cathode, a narrow Faraday dark space and a positive column extending to the anode. Doran (1968) detected several luminous fronts that were associated with the formation of a concentrated glow discharge and originated from the cathode and anode spots. After several avalanche generation periods an anode directed luminous front was observed followed immediately by an cathode directed front. The propagation velocity of these fronts was approximately 10^8 cm/s which he noted was an order of magnitude greater than the electron drift velocity. The Faraday dark space that separates the high field region at the cathode from the low field region of the positive column contracts and finally disappears. This is a characteristic of transient breakdowns when the energy supplied to the cathode fall region and the positive column is greater than that required for a stable glow discharge. This results in the heating of the gas in the vicinity of the cathode to produce a high temperature, high density plasma. The collapse of the Faraday dark space coincides with the end of the concentrated glow phase. A filamentary channel then forms which is very narrow as a consequence of the self-focusing properties of electron beams in a low pressure gas (Bennett, (1934)). This heralds the complete collapse of the applied voltage and the passage of a high current.

When a large overvoltage is applied to the discharge gap and if the initial avalanche carrier number in the mid–gap is sufficiently great, approximately 10^8, then no glow phases are observed. The only visible manifestation of breakdown is the formation of a filamentary discharge and the gap voltage collapses in a single step. The high current develops over a short period, less then 1 μs, during which the temperature in the spark channel is extremely high, 10,000–20,000 °K, and the intervening gas can be considered to be ionized to a large extent.

The formative time lag for a breakdown is dependent upon the magnitude of overvoltage. This is because the number of ionizations caused by electron collisions is very sensitive to the electrical field strength which in turn affects the formative time lag.

By applying a large overvoltage extremely short formative time lags of the order of 10^{-8} s have been achieved.

2.3 The experimental lamp

The lamp used in this project is a Samson LS–101 low inductance, high intensity, gas discharge EUV light source, and has been fully described in the U.S. Patent # 4,199,703 (Samson (1980)). The lamp in its most basic form, as seen from figure (2-4), is comprised of a water–cooled hollow cathode and anode, and an air–cooled electrically insulating ceramic cylinder. A gas flow is achieved by the gas being introduced at the distal end of the cathode, and a differential pumping system connected at the distal end of the anode. The hollow cathode is preferred to the plane cathode because for the same operating conditions a significantly increased production of highly energetic ion states is realised (as discussed above). The hollow anode is primarily designed for use when operating the lamp in the spark mode, where it provides an expansion chamber for the shock wave generated by the discharge to dissipate its energy. This minimizes the amount of dust, ceramic or electrode material from escaping into equipment attached to the lamp where they may cause damage. To prevent charged material form clogging the slits a set of six fins shaped into a quarter sector, are mounted in a radial configuration onto a plate that encloses the expansion chamber, and with their linear edge aligned to the optical axis as shown in figure (2-4). Because the electrical insulator cylinder is composed of a ceramic, the lamp can be operated at a much higher power level without the need for water–cooling. This eliminates the problem that occurs with conventional sources where the glass capillary can eventually break due to corrosion occurring when the lamp is run at high power levels. The main advantage of Samson's lamp is that it can be readily dismantled to allow examination and cleaning, and if necessary, replacement of any/all the electrode inserts and the discharge capillary (see below).

Samson's lamp embodies a characteristic similar to lamps designed by Newburgh et al (1962) and Paresce et al (1971), in that the negative glow is observed directly at the

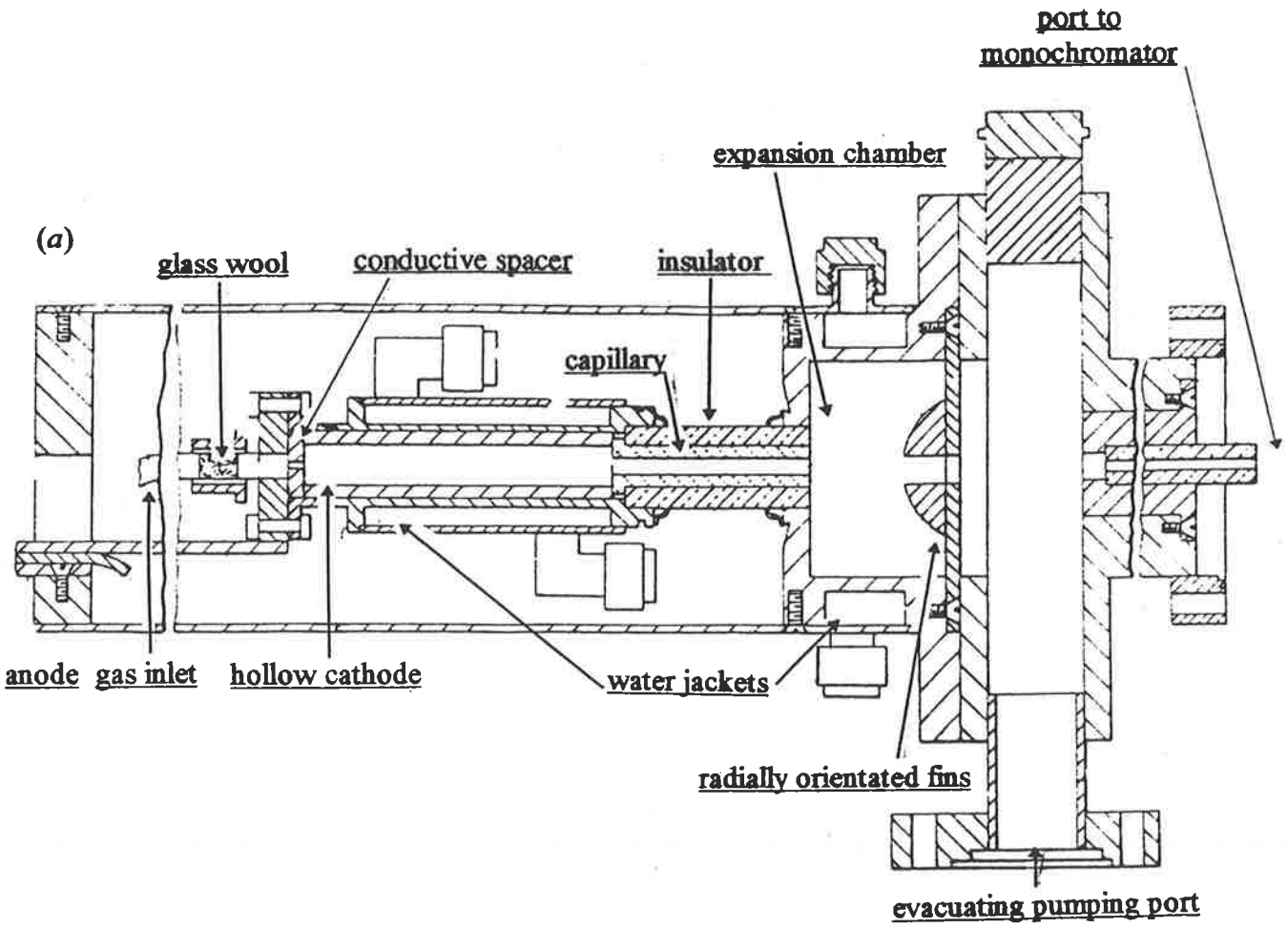

(b)

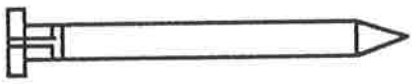

Figure (2-4). Samson's lamp, (*a*), with the important parts indicated. The conductive spacer from Samson's lamp was replaced with the one shown in, (b) (not drawn to scale) , for when the lamp was operated in the pulsed mode resulting in an improvement of the discharge as discussed in the text ((*a*), Samson (1980)).

exit slit of the lamp. This is achieved by substantially reducing the pressure in the lamp beyond the negative glow region resulting in a considerable reduction of self–absorption of the emission lines produced in the negative glow. This reduction of the pressure is attained by insertion of a 2 mm bore diameter discharge capillary into the ceramic cylinder, which impedes the gas flow. The capillary is constructed of boron nitride, a ceramic with superior electrical, thermal and machining properties. The small pumping conductance of the capillary also increases the pressure in the hollow cathode, permitting ignition of the lamp at lower voltages. To optimize the light output of the lamp the length of the capillary can be varied so as to be between 4 cm and 5 cm for a spark discharge, and at least 5 cm for a glow discharge.

The peak current through a discharge lamp is limited by the inductance of the lamp. Samson minimises his lamp's inductance by constructing both electrode and earthed shield surfaces to a cylindrical shape and with the shield positioned as close to the optical axis as practical. Discharge repetition rates between 10 and 100 Hz and with pulses up to 5000 volts and 3000 amps peak current are typical for operation in the spark discharge mode, which will produce intense ion emission spectra.

Because the pressure within the lamp is non–uniform, it is meaningless to speak of a single gas pressure within the lamp. However, as the exact nature of the discharge is pressure–dependent, it is instructive that it should be quantified in some manner. The pressure was measured in the differential pumping cavity between the lamp and the entrance slit assembly of the monochromator.

Samson's light source is capable of producing radiation from 90–6000 Å by modifications to the internal dimensions of the lamp and the lamp's power supply.

2.4 Lamp power supplies

The light source was operated by a dc or pulsed dc power supply, with figure (2-5) showing the circuit diagrams for both supplies. A dc voltage is produced by full wave rectification of a mains supplied transformer supplying a 20 KV, 200 mA output.

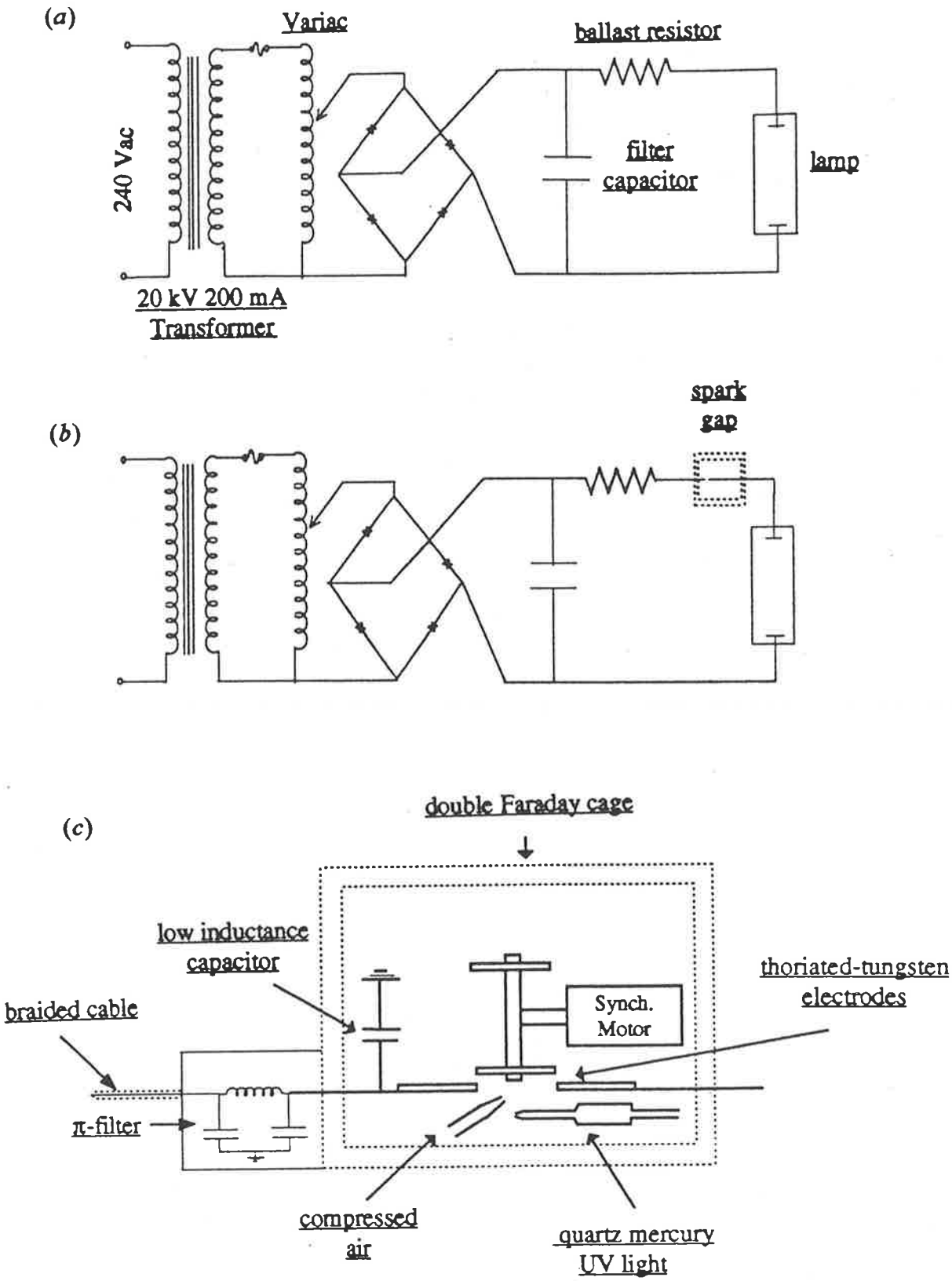

Figure (2-5). Diagram (*a*) and (*b*) displays a schematic of the dc and pulsed power supplies respectively. Diagram (*c*) shows a schematic of the rotary spark gap employed for the pulsed lamp.

Additionally a 1000 μF capacitor across the rectifier output reduced the ripple factor to approximately 10^{-3}.

The pulsed power supply is virtually identical to the dc power supply, with the inclusion of a rotary spark gap, a low inductance capacitor and a π-filter, as shown in figure (2-5). The rotary spark gap consists of four thoriated–tungsten rods, 3 mm diameter and 5 cm long, two of which are attached perpendicularly onto the end of a shaft that rotates about the spindle of a dc synchronous motor. The thoriated–tungsten rods were selected for their lower work function and therefore higher current delivery capabilities. The remaining two rods are fixed, parallel to the rods on the spindle and face each other end–on with a gap of 2 cm. One is connected to the low inductance capacitor, while the other is attached to the lamp via a flat transmission line (a parallel earthed second flat transmission line provides a low inductance connection to the lamp). The gaps between the moving and stationary electrodes were made as small as possible, (by using a piece of paper to set the gaps), to minimise the breakdown voltage across the gaps. The layout of the spark gap electrodes is identical to Samson (1967) and is superior to that of Cook and Metzger (1964), with the current flow across the gaps in opposing directions, thereby minimising the radiated electric and magnetic fields. Cook and Metzger (1964) increased the stability of their spark gap by illuminating the gap with the UV light from a quartz mercury pen–ray lamp, which facilitates the discharge across the gap. The operation of the spark gap is kept as smooth and electrically quiet as possible (see figure (2-5)) by removing the products of the discharge by blowing a stream of air across the gap. Repetition rates for the lamp were set at 30 Hz and the duration of the light pulse was of the order of 2 μs which is suitable for analogue detection (Samson 1967).

2.4.1 Lamp operation

The operation of the lamp was in accordance with the instruction manual as supplied by Minuteman Laboratories. Both the lamp and gas input line were pumped out by the differential pump until no discernible reduction in the pressure was observed,

typically about 100 mT as measured in the lamp. The water supply used to provide cooling for the lamp was turned on, and the cold finger in the differential pump line was immersed in liquid air. The use of the cold finger achieved two results. Firstly, it prevented outgassed oil from the rotary pump from back–leaking, therefore contaminating the lamp's internal surfaces, which can cause a diminution of the lamp's emission line intensities over a period of time. Secondly, the cold finger is a pump itself with a large pumping speed, as evident by the sudden drop in the lamp pressure (to ≤ 0 mT) when the liquid air was added to the cold finger. This facilitates the ignition of the lamp by allowing a higher pressure in the hollow cathode and furthermore reduces even further the level of self–absorption in the lamp.

The lamp and gas input line were flushed with helium several times before each experimental run and the pressure in the lamp adjusted by needle valve to approximately 0.1 mT. For operation of the lamp in the dc mode, the power supply was set to about 5 kV and when the lamp ignited, the voltage was reduced until the current through the lamp was approximately 150 mA.

The above pre–ignition procedures are applicable for the lamp to be also operated in the pulse mode. However, with the addition of the spark gap, modifications to the lamp were required. Difficulties were initially encountered when attempting to initiate a discharge, even with the power supply output increased to 10 kV. After consultation with Dr. McCoy, it was suggested that the substitution of the conductive spacer (see figure (2-4)) for a short pointed projection, (which would increase the electric field strength gradient near the point), should improve the chances of striking the lamp (see equation (2.5)). This proved to be the case. After initiating the discharge the voltage across the lamp was adjusted to 8.5 kV, which is approximately 140% of the breakdown voltage (5 kV for the lamp and 0.6 kV for the spark gap), with an average discharge current of approximately 150 mA. The lamp was operated with such a large overvoltage to produce a lower formative time lag for the initiation of the discharge and to eliminate the glow stages. The

latter should result in a narrower discharge filament in the lamp and produce the maximum ionized line intensities possible of the lamp's exit slit.

Another factor impacting on a successful firing of the pulsed lamp is the speed of the spark gap's rotor. The low inductance discharge capacitor must be permitted to charge up sufficiently to be able to supply the breakdown voltage to the lamp. Therefore it is accepted practice, (Samson (1967)), to operate the rotor at least several times the RC time constant of the power supply where R is the load resistance and C the capacitance of the low inductive capacitor. The RC time constant for this work is 0.6 ms corresponding to a rotor speed of 1666 Hz. This was well above the operating limits for the rotor used, and the spark gap was operated at 15 Hz resulting in the light pulse generated at 30 Hz and produced a large signal strength for the ion detectors.

Common problems associated with the pulsed spark discharge are the tendency of the discharge to take place in the gas inlet line, "back–firing", and the generation of electrical noise. The first problem was observed to cause instabilities in the light output which was quenched at times. This was resolved by inserting a glass wool plug directly behind the lamp's spacer, which successfully eliminated back–firing by decreasing the mean free path of the electron (Samson (1967)). The electrical noise radiating from the spark gap and the lamp was reduced by shielding both sources and also eliminating any radiating ground loops. Finally, the lamp was totally insulated from the monochromator by inserting a teflon flange between them and earthing the lamp at the power supply.

2.5 The Lamp spectra

The lamp was operated using helium gas to recreate some of the major solar emission lines in the EUV that impinge upon the earth's upper atmosphere. The lamp's spectrum was dependent upon the operational mode of the lamp. Common, however, to both modes is the fact that, as the source produces principally a discrete many–line spectrum, the scattered radiation and higher order emission lines can be easily identified.

For operation with a dc power supply the spectrum is characteristic of an atomic line spectrum with the most intense lines from transitions to the neutral ground state (He I), and with a very low scattered background consisting entirely of light below the ionization threshold (see figure (2-6)). To reduce the intensity of direct light entering the detection chamber a post–grating mask was used. The line spectrum associated with the pulsed condensed spark discharge results in the most intense lines being from transitions to the singly ionized ground state (He II), but with a background above the ionization threshold, that increases in intensity with a decreasing wavelength (see figure (2-6)). This stray background was shown by Blackwell et al (1966), who used a plane grating predisperser, to consist entirely of scattered light entering the detector, and so care must be taken when conducting absorption measurements to determine the level of ionizing radiation present in this scattered light.

The light intensity for the pulsed mode mirrors the current pulse profile, (Samson (1967)), which was observed on a C.R.O. The lamp's current temporal shape was naturally very similar to Samson's, and with the light pulse lasting approximately 2 μs, the resultant instantaneous current through the lamp was calculated to be approximately 2500 A.

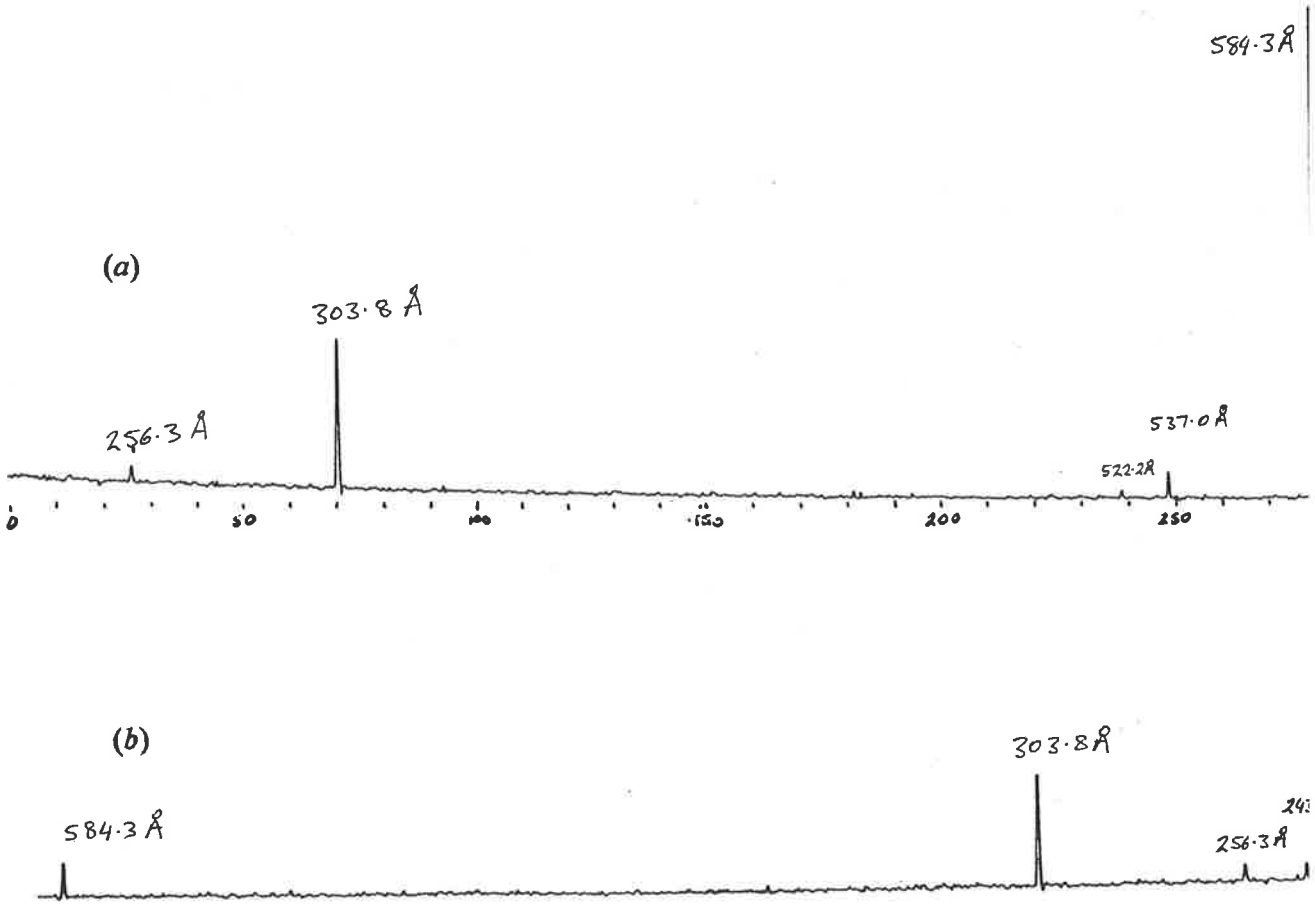

Figure (2-6). Plots of the dc, (*a*), and pulsed, (*b*), spectra with their important emission lines labelled.

CHAPTER 3

Wavelength selection

3.1 Diffraction grating theory

Samson (1967) presents a more than adequate account of the theory of diffraction gratings, however, I will tender a precis of reflection concave diffraction gratings as applicable to this work.

The fundamental principle of the concave diffraction grating is when the centre of the grating, exit and entrance slits are all placed strategically on the circumference of a Rowland circle, the diameter being equal to the radius of curvature of the grating, then the entrance slit's image will be focussed at the exit slit. Because of the extreme shortness of the wavelengths employed in this work, the grating must be used in a grazing incidence geometry to maximise the light intensity at the exit slit. Gratings are blazed so as to shift the concentration of light intensity away from the zeroth order and into a higher order of the spectrum, typically the first order. Blazing of the grating requires the grooves to be ruled, with the angle of the ruled face to the grating plane defining the blaze angle. Blazing results in the specularly reflected beam to coincide with one wavelength, known as the blazed wavelength. The blazed wavelength is specified for the first order, even though the same criteria apply for half the wavelength in the second order and one-third the wavelength in the third order and so on. The overlapping of higher orders can present a serious problem for continuum sources however blazing for the first order to give the highest possible free spectral range and the use of filters can help to negate this problem. Specifically for line sources, overlapping of higher orders is generally not a problem, particularly so for EUV sources.

3.2 The monochromator

The instrument used here is a GCA/McPherson model #247 grazing incidence monochromator. Figure (3-1) illustrates the basic components of the monochromator, where the movable elements are limited to one component, the entrance slit, to minimise defocussing of the slit image. The Bausch and Lomb replica grating is concave, with a 2217·6 mm radius, and is ruled with 1200 grooves per mm. The ruled area measures 50 mm wide, with a groove length of 30 mm, and with a blaze angle of 2°4′ the blaze wavelength is 600 Å. The exit slit was set at an angle of 84° relative to the normal of the grating plane, theoretically producing an effective wavelength range for the monochromator of 0 to 592 Å. A number read off the monochromator's scanning position indicator provides the cord distance, in inches, from the entrance slit to the grating's centre. This can be easily converted to provide the wavelength of the light at the monochromator's exit slit by conferring with the counter reading versus wavelength chart, or more accurately from a catalogued equation, both of which are contained in the GCA/McPherson user's manual. However, as the light source for this project produces resonant radiation that is peculiar to the lamp's gas filling the wavelengths of the emission lines can be easily matched with those listed in atomic or molecular wavelength tables.

The choice of a line emission over a continuum source for absorption studies negates problems associated with the instrumental bandwidth and its impact on the measured absorption cross section. Critically speaking, this is only true for a constant and smooth absorption curve, which is generally the case for absorption in the EUV, over the monochromator's bandwidth function. Therefore in this work it is not crucial for the slit function to be a symmetrical triangular function, (see Hudson and Carter (1968)). This allows the slit widths to be determined independently, with a resultant trapezoidal shaped slit function, which will optimize the light output at the exit slit without exceeding the maximum permissible pressure levels in the monochromator. EUV gas discharge sources are typically of low intensity so the entrance slit was used as wide as practicable. The entrance slit width selected was 250 μ with the resultant pressure in the monochromator being approximately 5×10^{-5} T. An exit slit width of 1,000 μ maximised the light intensity

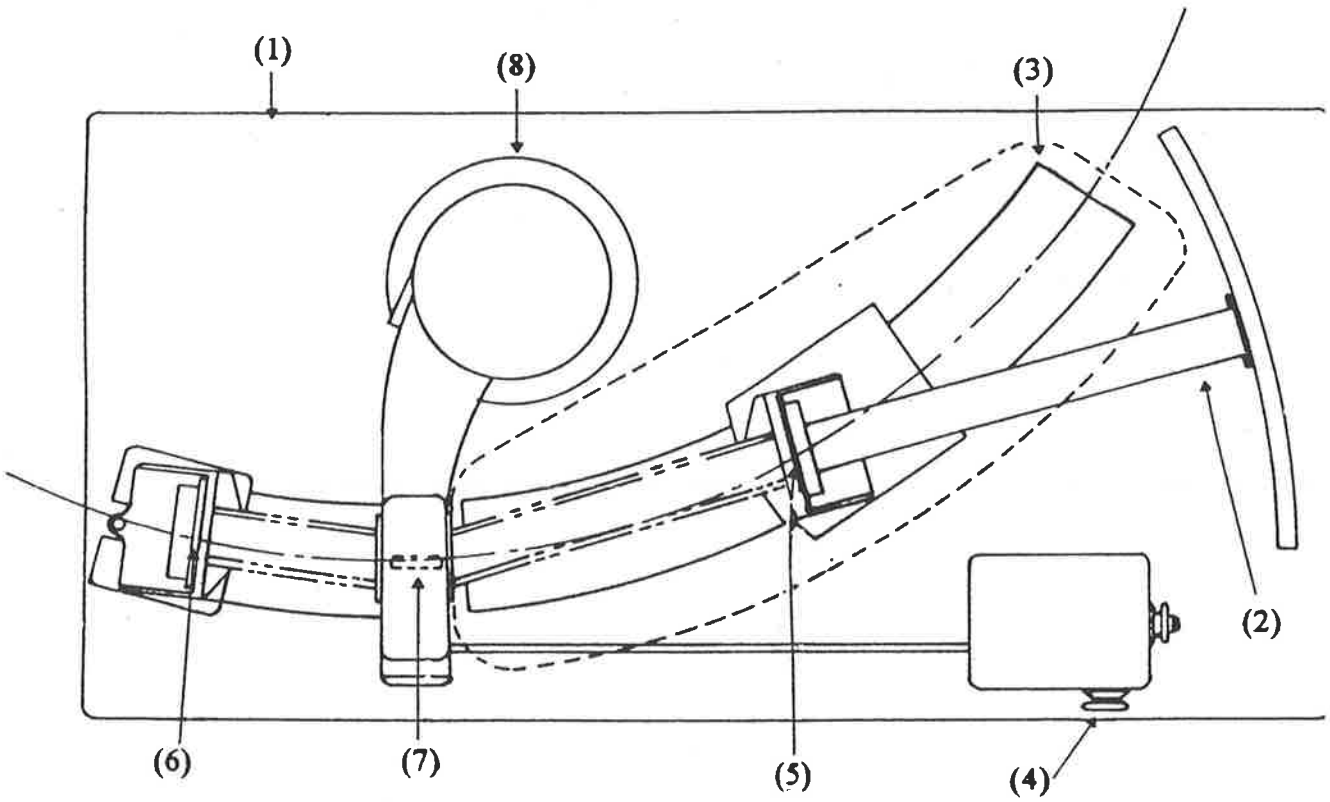

Figure (3-1). Schematic diagram of the McPherson model 247 grazing incidence monochromator with the following attributes labelled- (1)- granite base, (2)- straight edge, (3)- curved way,(4)- wavelength scan control,(5)- scanning entrance slit, (6)- non-scanning exit slit (7)- grating, (8)- main vacuum chamber (GCA/McPherson (1968)).

at the exit slit with a negligible amount of target gas from the detector chamber detected in the monochromator, (never exceeding 2×10^{-5} T). This was only achievable after a flange with a 1 cm by 0.3 cm slit was inserted between the differential pumping port and the monochromator. The wavelength resolution for this work is independent of the monochromator slits' settings, as the light source produces isolated emission lines. Instead the resolution is dependent on the line widths produced by the H.C. lamp, which is approximately 0·001 Å (Samson (1967)).

3.3 Operation of the monochromator

The monochromator was operated in the scanning mode with the entrance slit mounted onto a curved way, that tracks with the grating's Rowland circle. The lamp is mated to the monochromator's entrance slit and is positioned on the curved way using the wavelength drive mechanism, as shown in figure (3-1). The wavelength of the light emerging from the monochromator is simply adjusted by operating the scanning controller to move the lamp along the curved way, thereby altering the angle of the entrance slit to the grating.

The general running of the monochromator included maintenance of the roughing and diffusion pumps. This entailed examining, and when necessary changing the pump fluids because of a build–up of contaminants which leads to a reduced pumping speed. Of particular concern is the accumulation of deposits onto the grating surface. With irradiation by EUV light they will over time react with and destroy the surface of the grating. McPherson's manual includes a technical bulletin with their suggested method for cleaning a grating, however I found this to be less than satisfactory. CSIRO's Division of Chemical Physics has developed a superior method, with the application of a resin solution onto the grating surface. When this resin has nearly dried it can be easily peeled off, along with any loosely bonded contaminants from the grating surface. I have no data to confirm any improvements in the performance of the grating after cleaning with the resin, however, the grating appeared cleaner to the naked eye.

CHAPTER 4

Ionization particle detectors

4.1 Double ionization chamber theory

The absorption of monochromatic radiation by a gas can be quantified with the equation (also known as Beer's law),

$$I = I_0 e^{(-n\sigma L)} \qquad (4.1)$$

where I_0 and I are the photon fluxes entering and emerging from the interaction region respectively, n is the number density of the target gas, L is the path length of the interaction region and σ is the total absorption cross section of the gas.

For radiation whose energy is greater than the first ionization threshold of the gas, an ionization chamber with an appropriate voltage applied across the plates can be used for the detection of ionic fragments. An ionization chamber, however, can not by itself discriminate between atomic, or molecular, ground, excited, or dissociated state, ions. Single ion collector plates were initially used, but later modifications included double collector plates (Wainfan et al (1953)), installed in tandem and with grounded guard electrodes. Watanabe (1954) omitted the guard electrodes and extended the two collector plates so that they occupied the entire length of the ion chamber. By situating the plates so that they almost touch at the chambers midpoint simplifies the computation of the cross section (figure (4-1)).

The chief advantage of using a double ionization chamber ("ion chamber") instead of traditional absorption systems for cross sectional measurements is that the two ion currents are measured simultaneously. This eliminates errors due to temporal variations in the light output from the lamp and/or the pressure and\or the temperature of the target gas in the ion chamber. Additionally the ion chamber is insensitive to scattered radiation of wavelengths longer than the first ionization threshold of the target gas. Scattered radiation

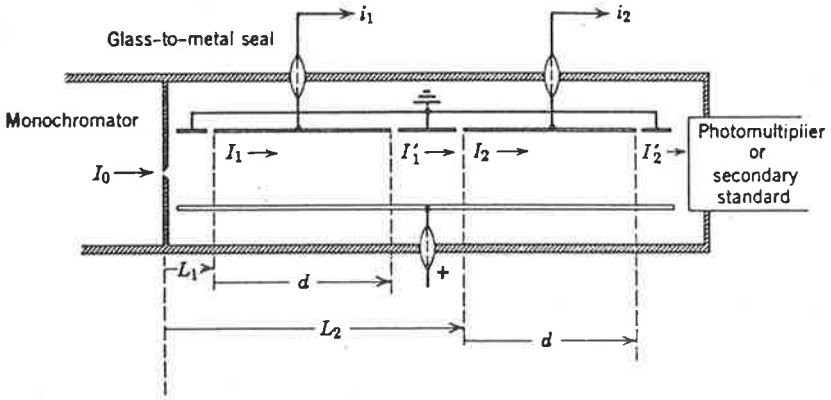

Figure (4-1). Double ionization chamber (Samson (1964a)).

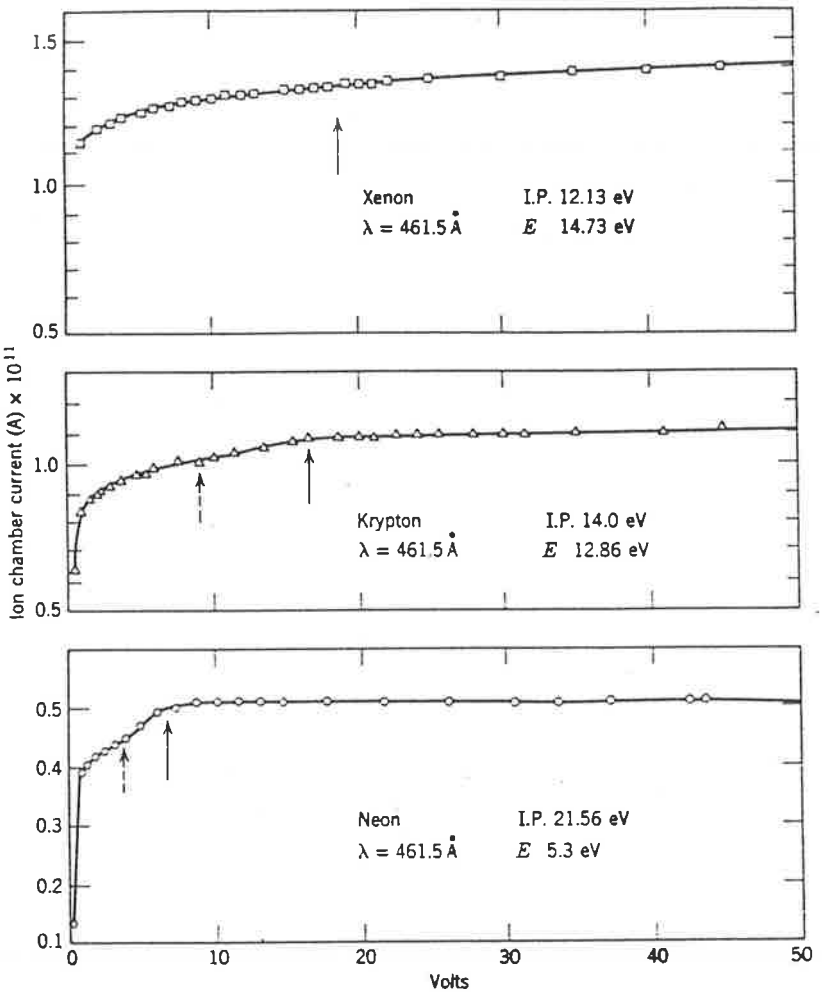

Figure (4-2). The above plots show the ion currents as function of applied repulsive voltage. The series show the dependence for firstly the existence and secondly the position of the plateau on the ionization potential of the target gas and the applied repulsive voltage. The dashed lines marks the onset, and the solid line the completion, of electron retardation. (Samson (1964a)).

and over–lapping higher order spectra is respectively reduced or effectively eliminated here because a line source was used. Cook and Metzger (1964) investigated the effect of fluorescent radiation on the measurement of cross sections between 600–1000 Å for oxygen and nitrogen and concluded that the wavelength of such radiation was longer than 3000 Å.

For wavelengths shorter than 1000Å there are no transparent window materials available. As the intensity of EUV gas discharge line sources are notoriously weak, partially transparent windows are not a viable option. The ion chamber must therefore be operated in the windowless mode, with a constant leaking of the target gas through the chamber's entrance slit and a controlled gas replenishment system. A differential pumping system is used to remove the gas before it can enter the monochromator. With such a dynamic gas flow it is imperative that no pressure fluctuations exist within the ion chamber which would result in an erroneous measurement of the cross section. Cook and Metzger (1964) experimented by varying the positions of the gas inlet port and the pressure measuring devices along the ion chamber length finding no variance of their respective measurements of the pressure readings and the cross sections.

Positive ions are formed with their initial thermal energy, approximately 0.025 eV at room temperature, that they possessed before the photoionizing interaction intact, due to their excessive mass relative to the electron, and supplemented with energy gained from the applied electric field. As mentioned before, a neutral or ion would have to attain double the first ionization potential before it could collide with and ionize a gas neutral. In contrast photoelectrons are ejected with an initial energy given by $E = h\nu - E_i$, where $h\nu$ is the photon energy and E_i the ionization threshold of the target gas, so the photoelectron can realistically possess several eV. An erroneously high electron current may be measured because the initial photoelectron may possess and/or gain enough energy from the electric field to ionize a gas atom with the secondary electron also drawn to their collector electrode. The repulsion electrode of the ion chamber is therefore biased positive to the collectors so as to repel the ions and sweep–up the electrons.

Sommerfield (1930) showed that the probability of an electron being ejected at an angle θ to the direction of propagation of the incident radiation is $\sin^2\theta$ so the most likely path of a photoelectron is perpendicular to the path of the incident radiation. Electrons travelling at an angle to, but opposing, the electric field lines are retarded at a lower voltage than electrons moving parallel to, but opposing, the field lines. With no repulsion field the collector electrode will be bombarded by equal numbers of electrons and ions. Incrementing the repulsion field will prevent electrons moving in the direction of the collector, at an ever decreasing angle to the field lines, from reaching the collector. Then the number of electrons moving towards the collector will decrease with increasing field strength until eventually no electrons will reach the collectors, (see figure (4-2)), and a "plateau" is attained in the measured ion current. Ideally the light beam is made to pass as close to the ion repeller plate as possible to minimise the number of electrons from reaching the ion collector and to also minimise the energy imparted to the electrons by the electric field to help prevent further ionizations. With higher photon energies the chamber preferably is modified to contend with the more highly energetic photoelectrons by surrounding the light beam with the repeller electrode and reducing the solid angle of the collector electrode, by replacing the plane ion collector with a rod ion collector, as seen by the photoelectrons and any scattered radiation (Cole and Dexter, (1977)). It is not critical for all the ions to be collected for cross section measurements as the ratio of the front to back ion currents is constant with a varying repeller voltage (Samson, (1967)). However maximising the ion currents detected, for either a low ionization cross section or low intensity lamp emission line, will improve the quality of the data. For calculations of the photoionization yield or the absolute photon flux it is, however, imperative that the plateau has been reached to ensure that all primary ions formed are collected and no photoelectrons impinge on the collectors.

Samson and Yin (1989) investigated systematic errors associated with the use of their ion chamber design and how such errors effected the accuracy of cross section measurements. Their solutions resulted in a quoted total accumulated error in their

measurement of the total photoionization cross section of ± 0.8 %. A concise examination of the systematic errors investigated by Samson and Yin is found in Appendix I.

4.2 The experimental double ion chamber

The ion chamber used for this project is illustrated in figure (4-3) and incorporates the advantages described in the previous section and in Appendix I. The interaction region is almost fully enclosed by the stainless steel repeller shield. The entrance aperture to the ion chamber measures 15 mm by 0.5 mm. Using a low vapour pressure glue, a rubber O–ring was glued onto the outside surface of the entrance slit face and the ion chamber situated so that the O–ring was abut to the vacuum chamber that encompasses the ion chamber. This compels the target gas to flow through the entrance slit and so prevent pressure fluctuations within the ion chamber. The O–ring was necessary to insulate the repeller field electrode from the earthed monochromator. The ion chamber was terminated with a 90 % transmission stainless steel mesh to allow the light beam to be absorbed by the sodium salicylate, a VUV fluorescent material, coated perspex light pipe. An EMI 9514S photomultiplier (the S-type photomultiplier cathodes are most sensitive near the 4250 Å maximum emission from the sodium salicylate) is used to locate the lamp's emission lines. The divergence of the light beam was measured in both the horizontal and vertical directions to be less than 0.5°. The low beam divergence permits the distance between the repeller electrode and the beam axis to be only 2 cm to minimise secondary ionization. This can be easily achieved by constructing the ion chamber with a rectangular cross section.

A low conductance baffle slit was constructed and placed at the entrance of the vacuum chamber, adjacent to the monochromator's exit slit, housing the ion chamber (see figure (4-4)). This enabled target gas pressures up to 250 mT in the ion chamber whilst limiting the pressure in the monochromator to approximately 10^{-5} T. The baffle slit also helps to reduce the amount of scattered light entering the ion chamber. The dimensions of the baffle slit was determined from the effective pumping speed at the differentially pumped region and the ultimate pressures required for the ion chamber and the

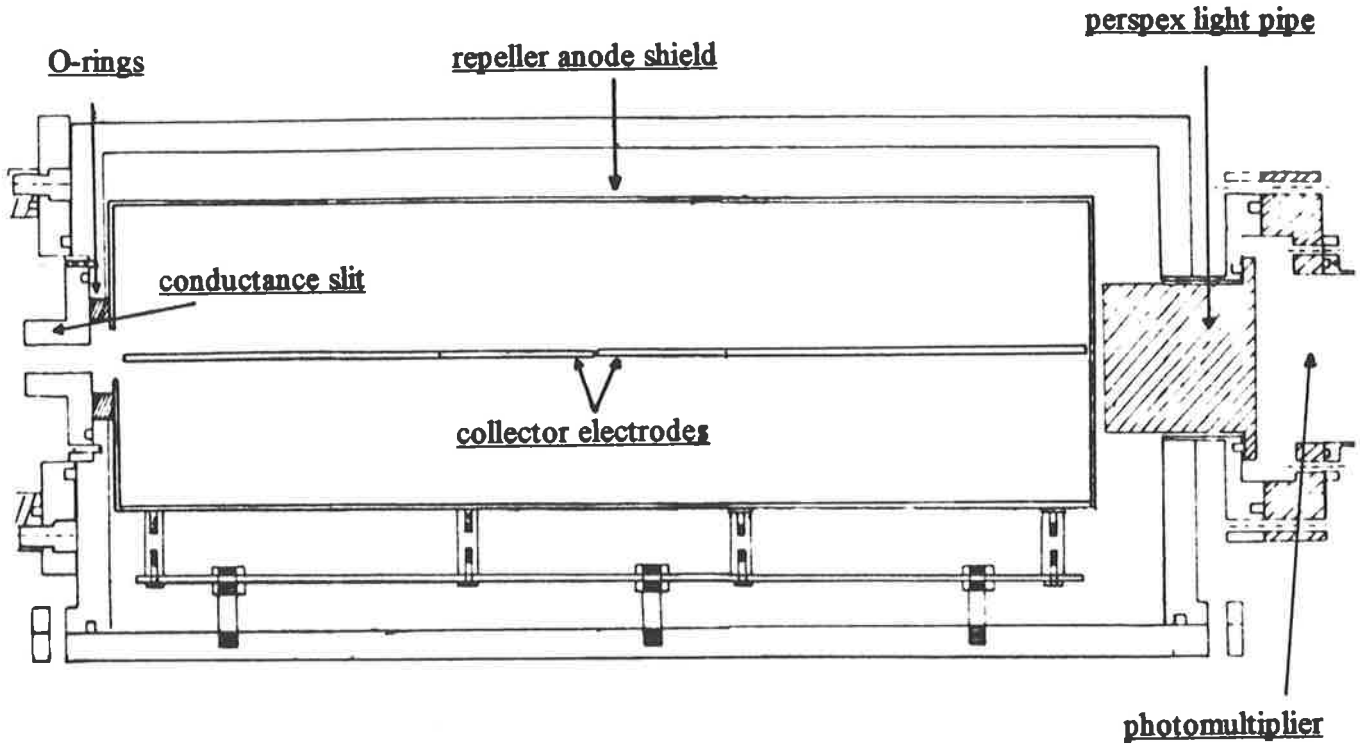

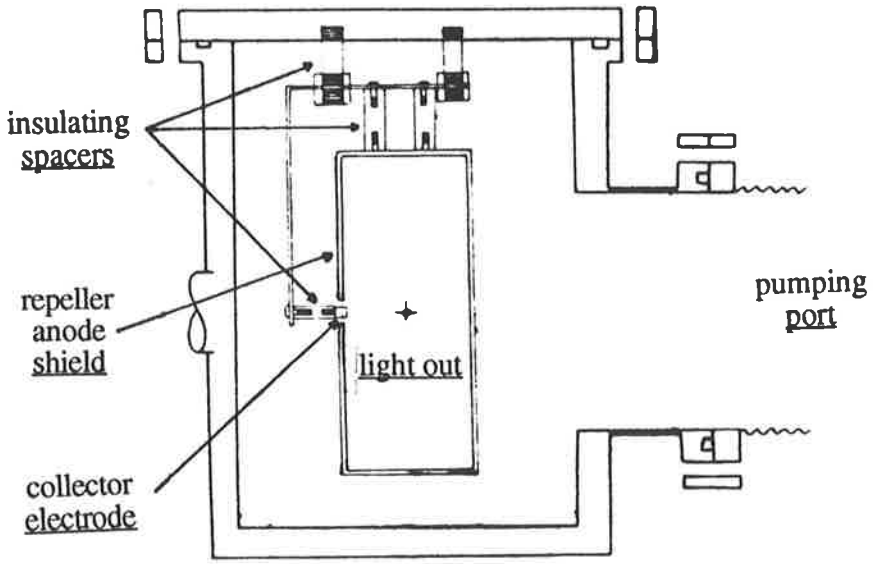

Figure (4-3). The experimental double ion chamber shown from a side and end on view.

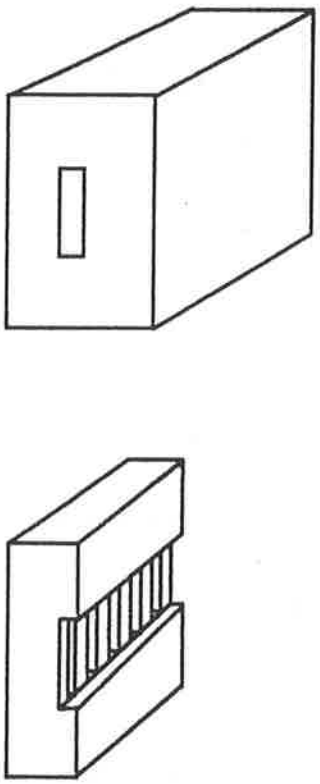

Figure (4-4). Low conductance slit for the ion chamber. The total width of the groves are alternatively 0.1 and 0.3 cm. The final construction was secured onto a circular flange so as to enable the slit to mounted to the entrance slit of the double ion chamber' vacuum chamber (see figure 4-3).

monochromator and calculated from an equation in Samson (1967). The exit slit width of the monochromator is 1 mm, so a minimum baffle slit width of 2 mm was chosen to prevent any significant reduction of the intensity of the light beam.

The majority of electrical insulation for the ion chamber was achieved by using teflon lugs between the electrical conductors. Teflon has excellent resistance and vacuum properties. The ion chamber is suspended from the vacuum chamber's upper flange via teflon lugs. The ion collectors are connected by ceramic lugs to a stainless steel support, which is supported by teflon lugs to the vacuum chamber. Teflon was not used to support the ion collector rods as it can generate currents, when put under stress, in the picoampere range. Using approximated lamp intensities and quoted cross section values from the literature, the ion currents were expected to range from 10^{-12} to 10^{-10} A, so the ion chamber's insulation lugs were required to have very small leakage currents. This was achieved by ensuring that the ion chamber was scrupulously cleaned before each data collection run. Because the major source of contamination is oil from the pumping systems, the assembled ion chamber was first washed in a tetrachloride "rain" shower. This was produced by heating tetrachloride in a frying pan with a water cooled jacket used to condense the vapour into a rain shower above the ion chamber, to dissolve oil contaminates from the ion chamber surfaces. Acetone was then sprayed on to wash any remaining oil away. Methanol spray then removed any water and finally ethanol rinsed away any residual acetone or methanol. Only research grade chemicals were used in cleaning the ion chamber, thereby minimising any further contamination.

Current signals from the collector electrodes were carried along single strand teflon insulated wires, to minimise movement, to the ion chamber's vacuum housing and transmitted to the outside world via doubly–shielded kodar–kovar feed–throughs. The guard electrode is held at the same potential as the data electrode (earth), thereby intercepting any transient noise currents. The battery powered repulsion field voltage was passed into the ion chamber's vacuum chamber by a glass feed–through and relayed along a PVC coated wire.

4.3 Photoionization cross section measurements using the double ionization chamber

Let I_0, I_1 and I_2 be the photon fluxes at the entrance, midpoint and exit of the ion chamber respectively and assume that the ion collectors, of length L, meet in the chamber's midpoint, as shown in figure (4-3). Then for the front ion chamber

$$I_0 = I_1 e^{(n\sigma L)} \tag{4.2}$$

and the total current from the front chamber is then given by

$$i_1 = (I_0 - I_1)\,\gamma\, e \tag{4.3}$$

where γ is the photoionization yield and e the charge of an electron. Then combining equations (4.2) with (4.3) gives

$$i_1 = I_1 (e^{(n\sigma L)} - 1) \tag{4.4}$$

and similarly for the back chamber

$$I_1 = I_2 e^{(n\sigma L)} \tag{4.5}$$

and

$$i_2 = I_2 (e^{(n\sigma L)} - 1) \tag{4.6}$$

Then combining equations (4.6), (4.4) and (4.5) and with some simple manipulation results in the total photoionization cross section equation for the ion chamber to be given as

$$\sigma = \frac{\ln\left(\frac{i_1}{i_2}\right)}{n L} \qquad (4.7)$$

The total photoionization cross section can then be determined by measuring the front and back ion currents, the length of the collectors and the number density of the gas in the ion chamber.

4.4 Metrology of the experimental ion chamber

This entailed the determination of the length of the ion collection region and the number density of the target gas in the ion chamber. To ensure that the most accurate measurement of the cross section was realised, the systematic errors associated with the determination of the cross section in relation to the ion chamber's experimental variables are discussed.

4.4.1 Determination of ion collector length

To simplify the cross section measurements the ion chamber is bisected to form the double ion chamber, making equation (4.7) expedient. It is not crucial for the two ion collector electrodes to be exactly of equal length, but it is imperative that they meet precisely at the centre of the ion chamber, with the gap as small as possible. This was achieved by using a piece of paper to fix the gap to 0.15 mm. Any error in the ion collector length can then be reasonably attributed to the accuracy in determining the centre of the ion chamber.

The inner chamber face of the entrance slit defines the onset of the collecting region for the ion chamber. Likewise the inner chamber surface of the 90 % transmission mesh defines the end of the ion chamber ion collection region (see Appendix I). The length of the ion chamber, 2L, was measured with a vernier calliper to be 308.80 mm, giving L equal to 154.40 mm. The centre of the ion chamber was marked with a scribe to within an estimated error of ± 0.1 mm, this being half the width of the scriber's mark. A

further error for the positioning of the two collector electrodes about this central point was estimated to also be ± 0.1 mm. Then the total error in L is ± 0.2 mm.

4.4.2 Determination of the number density

The number density of the target gas was calculated from the gas pressure and temperature which are determined independently.

4.4.2(a) Temperature measurement

This was measured indirectly using a precision IC temperature sensor (National Semiconductor LM35 chip) with the vacuum chamber housing the ion chamber being the heat sink for the chip's metal can package. The chip's operational range is quoted in it's specification sheets as –55 to +150° C. The temperature of the vacuum housing was averaged from that recorded before and after each experimental run to avoid interference from the electromagnetic noise radiating from the lamp and the spark gap. The chip and associated circuit was calibrated using iced water, by averaging the temperature recorded every minute over a 30 minute period, to be (0.03 ± 0.001)°C. This excellent result was expected as the manufacturer's specification sheet states that the chip's accuracy is guaranteed to ± 0.5°C (at 25°C) for any given single measurement and therefore does not require any external calibration or trimming.

A final point to consider is the cooling of the target gas upon free expansion, otherwise known as a Joule–Kelvin expansion, when admitted into the vacuum chamber from the reservoir, where the gas is stored slightly above atmospheric pressure. Using their respective virial coefficients the temperature drop for a Joule–Kelvin expansion for argon, oxygen and nitrogen are 2.75, 2.81 and 2.65 °K respectively. However Dr. McCoy pointed out that the gas temperature would reach equilibrium with the vacuum chamber in a very short time. In any case the temperature of the gas would reach equilibrium with the equipment after the two hour period required for the pressure in the ion chamber to stabilise.

4.4.2(b) Pressure measurement

The pressure of the target gas in the ion chamber was measured with a MKS Baratron type 220B capacitance manometer using a 1 Torr head. The pressure transducer is an absolute unit with a metal diaphragm separating the sealed and gettered high vacuum reference cavity (at 10^{-7} T) from the port attached to the ion chamber's vacuum chamber. The unit also contains a heater circuit to maintain the sensor at an internally regulated temperature to ensure it's accuracy and with the unit operated in a temperature controlled environment, temperature transpiration effects are totally eliminated (Gascoigne (1970)). The manufacturer's instruction manual states the linearity of the pressure measurement at $\pm$ 0.15 % and with a temperature coefficient of $\pm$ 0.02 % /°C the final relative error of the pressure measurement could be assumed to be $\pm$ 0.17 %. However, Samson and Yin (1989) constructed a precision oil manometer to recalibrate their capacitance manometer, which they found read 0.72 % too high. Attempts to calibrate the capacitance manometer to be used for this experiment were fruitless as the only standard available was a McLeod gauge which could not provide repeatable results over four calibration runs. Assigning a realistic total error for the pressure measurement is therefore a difficult task.

The dc output from the Baratron transducer was used to control the flow rate of the target gas into the ion chamber through a needle valve. It is firstly necessary to zero the Baratron gauge by pumping to below the gauge minimum, in this case 0.1 mT, and then after a 30 minute warm–up period the zero potentiometer is adjusted so that the pressure meter reads zero. The pressure gauge supplies a 10 V output which was used as an input into a Granville–Phillip's automatic pressure controller (APC). The APC subsequently operates a servo driven valve by comparing the pressure in the vacuum chamber with the preset target pressure on the APC's reference control. The derivative and gain controls of the APC were adjusted so as to achieve a stable gas pressure to 0.1 mT during all of the cross section measurements. Typically the APC required several hours for the vacuum chamber's pressure to satisfactorily stabilise before attempting a cross section measurement. The target gases were supplied by CIG and were guaranteed at 99.95% pure.

4.4.4(c) Target gas number density

The number density can be easily deduced from the perfect gas law and is given by

$$n\,(cm^{-3}) = \frac{P\,(mT)}{T\,(^{\circ}K)} \times 9.653 \times 10^{15} \qquad (4.8)$$

CHAPTER 5

Ion current measuring equipment

5.1 Review of electrometer instrumentation

As stated before, the ion currents were expected to range from approximately 10^{-12} to 10^{-10} A. Therefore, to ensure an optimal precision for the cross section measurements, notwithstanding other sources of errors, the dark current for the ion detection equipment must be no greater than approximately 10^{-14} A.

Particular care is required when measuring extremely small currents because of the high input impedance and sensitivity of the current sensing equipment, such as with monolithic electrometers, that is operational amplifiers. Leakage current paths across printed circuit boards and the discrete components themselves can place severe limitations on both the accuracy and precision of the measurements. After components have been soldered in position, the printed circuit boards must be thoroughly cleaned using trichloroethylene to remove solder flux. The board is then rinsed with methanol, to remove any other residues, which evaporates without leaving a conducting deposit.

The inputs to the amplifier must be well shielded from stray currents, such as those originating from adjacent voltage supply pins. This can be simply achieved by incorporating an input guard ring on the circuit board which encircles the inputs with a conductor track that is driven to the same potential as the amplifier's inputs. The guard ring intercepts and so diverts any stray currents from reaching the amplifier's inputs. To further increase the degree of screening both sides of the circuit board are left with the largest area of a copper plane as possible. Another excellent method to protect the inputs from stray currents is to use ceramic insulated stand–offs. The current signal wires from the doubly–insulated feed–throughs to the amplifier inputs should be provided with their own shields that are driven to ground at one end only, preferably that end closest to the amplifier's input guard. The coaxial wire should have an adequate insulation, ideally teflon, and therefore be held rigid. Ground loops, such as one formed when the circuit's

power supply and amplifiers are not earthed at the one point on the circuit board, must be eliminated. The presence of a ground loop permits stray magnetic field pick–up, for example from those emanating from an electrically noisy circuit, such as a spark gap, or even from an ac powered instrument. The resultant induced voltage appearing at the amplifier's input has a magnitude dependent upon the area of the ground loop, the magnetic flux density and the orientation of the loop to the field lines.

5.2 Experimental electrometer

The methods discussed above were adhered to using a hybrid operational amplifier, the ultra low bias current Intel ICH8500 ACTV chip in a TO-99 metal package, with an input bias current less than 10^{-14} A when its metal case is driven to the same potential as the inputs. The chip consists of two closely matched MOSFETs employed as an input stage and encapsulated in the same package as a conventional operational amplifier without its normal input stage. The inputs are protected from voltage transients by, two internally opposed diodes which under normal operating conditions no voltage appears across the diodes and hence contributes no error current, and an external resistor in series to the amplifier's signal input pin. The circuit diagrams for an electrometer, with one used with each ion collector, is shown in figure (5-1). The circuit configuration chosen was the feedback type in preference to the shunt configuration as the input impedance and capacitance of the former is lower (Zsdanszky, 1973). The lower input impedance reduces insulation requirements and a significantly lower input capacitance results in a controlled rise time of the electrometer which is dependent upon the feedback resistance and capacitance. The discrete components on the circuit board are a source of errors and they must be individually substantiated to determine the best choice of components and method of usage. The Welwyn "Welmegox" composition type glass encapsulated resistor is the most suitable for use in the feedback circuit, with it's linearity being measured to be within ±1 % over a period of one year (Reid (1977)). It's stability to temperature and applied voltage variations is satisfactory with a temperature coefficient of < 0.5 % /°C and a voltage coefficient of < 0.25 % /V. Any movement or vibration produces a change in the

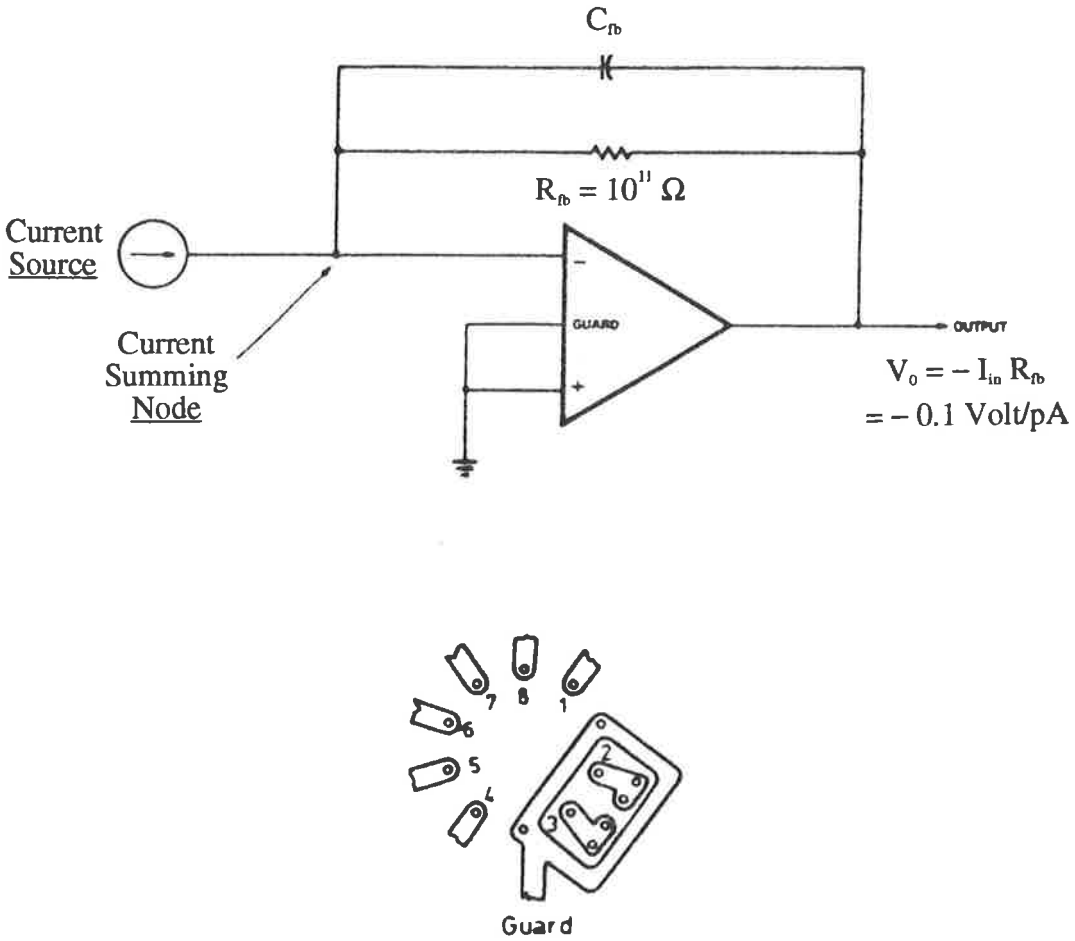

Figure (5-1). Single picoammeter schematic circuit (Intersil (1982) and a printed circuit board showing the input guard for the ICH8500/ACT (Clayton and Newby, (1992)).

capacitance across the feedback resistor and results in a corresponding transience in the output voltage, therefore the feedback resistor must be rigidly supported (Kerridge (1991)). For example, it can be clad inside a cylindrical short length of teflon with a rigid wire wrapped tightly over the teflon and both ends soldered onto the board. A capacitor in the feedback circuit can be used to reduce the bandwidth, and therefore the noise, of the amplifier. Current leakage across the surface of the feedback capacitor can be minimised by cleaning with methanol. A ceramic capacitor reduces the area of the dielectric therefore minimising the current leakage. A Welmegox $10^{11}\Omega$ resistor and a 1 pF ceramic capacitor form the feedback circuit giving the time constant for the electrometer equal to 0.1 s, therefore the output voltage has stabilized to within 1 % of its final voltage after half a second. To ensure effective screening from electromagnetic interference, the circuit board is mounted adjacent to the ion chamber's doubly insulated feed throughs with both housed in a metal box screwed to the top of the vacuum chamber. The operational amplifier's output is transmitted by wire to the digitising circuit which can increase the capacitive load of the output, resulting in the output oscillating. This was prevented by isolating this capacitive load from the amplifier's output with a series resistor at the amplifier output, R_o as shown in figure (5-1).

5.3 Digitiser circuit

The digitiser consists of a monolithic voltage to frequency converter, "V–F", an Analogue Device integrated circuit AD537, that accepts full scale input voltages of ± 30 V and provides an output up to 100 kHz, the maximum frequency depending upon the external RC network chosen. Linearity of the chip is rated at ± 0.05 % for 10 kHz full scale and provides a TTL output that is suitable to drive a LED. The RC combination chosen,(10 kΩ and 0.01 μF), ensures that for a 10 V (which is the maximum voltage output for the electrometers) input to the V-F chip results in a 10 kHz output. To prevent erroneous signals appearing at the high input impedance of the V–F, it's shielded from any electrical noise by enclosing it in the solid brass box that also encloses the boxed electrometers. The V–F's data signals are communicated to the outside world using

optocoupling techniques, a LED–phototransistor pair. Lying flush and in electrical contact with the wall of the shield box and positioned between the LED–phototransistor pair is a 90 % transmission mesh, which prevents electrical interference from penetrating the shield. The signal from the phototransistor is transmitted over a coaxial cable within copper tube shield, with the coaxial's shield grounded to the double Faraday cage that houses the computer, interface box and the APC. The signal wire, once inside the Faraday cage, is inputted into a high precision comparator chip (National Semiconductor LM 339) to modulate the pulses to TTL specifications, as required at the input to the computer interface circuit. Figure (5-2) shows the digitising circuitry and the LED–phototransistor construction.

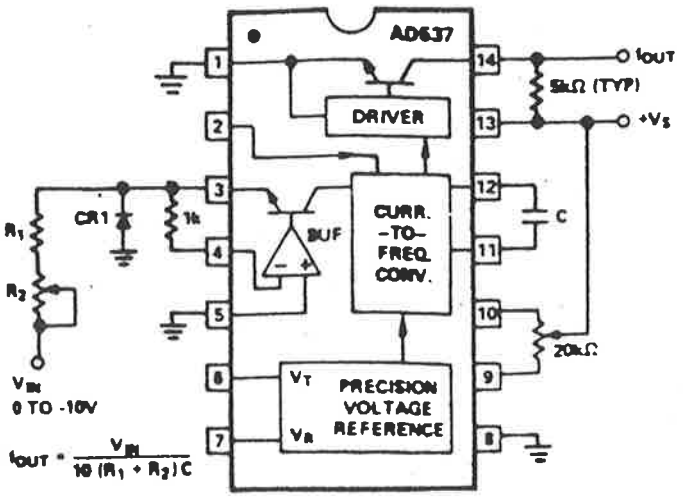

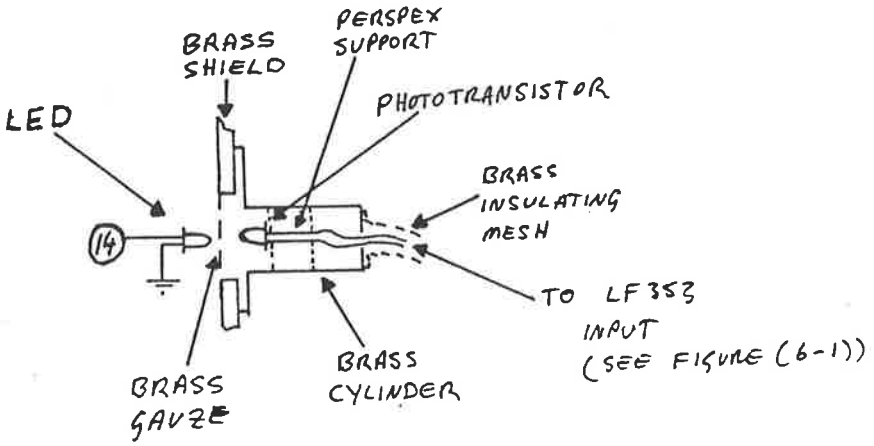

Figure (5-2). AD537 voltage to frequency chip circuit for use with negative input voltages (Analogue devices (1976)), and the LED/phototransistor set-up.

CHAPTER 6

Data recording electronics

6.1 Computer interface

The computer interface provides hand–shaking capabilities between the computer and an external electronic device, enabling storage of data which can be easily manipulated by computer software for later analysis. For the present work the interface permitted the computer to indirectly measure the two ion currents from the ion chamber by counting pulses (the frequency of which are shown below to be directly proportional to the ion currents) provided to the interface. The computer used here is a Commodore PET 8032.

The computer interface circuit is shown in Figure (6-1). The Rockwell R6522 Versatile Interface Adaptor (VIA) is the "brains" of the interface board with control of peripheral devices handled by its two programmable 8–bit bi–directional ports. Expanded hand–shaking capabilities enable controlled data transference between the peripheral devices and the microprocessor. The actual counting of the data pulses is executed by an Intel 8253 programmable interval timer which contains three independent pre–settable 16–bit down counters. The counters have separate inputs but are controlled by the same window pulse, whose period is set by counter #2 in the 8253 and can range from 2 μs to over 2 hours. The R6522 control lines, CA1 and CA2, are used to initiate the gating of the data to the counters in the 8253 chip. The initial count value, 65535, is programmed into the chip via a control word before the start of each data collection and with mode "0" selected, the 8253 is operated in the timer mode. The counters are latched to the VIA's ports by read handshaking which allows positive control of data transfer from the counters to the microprocessor. The direction of the data transfer is controlled by the R/W line in conjunction with the chip select inputs, CS1 and CS2. When R/W is high (read operation) and the R6522 is selected, data is transferred from the selected R6522 register onto the

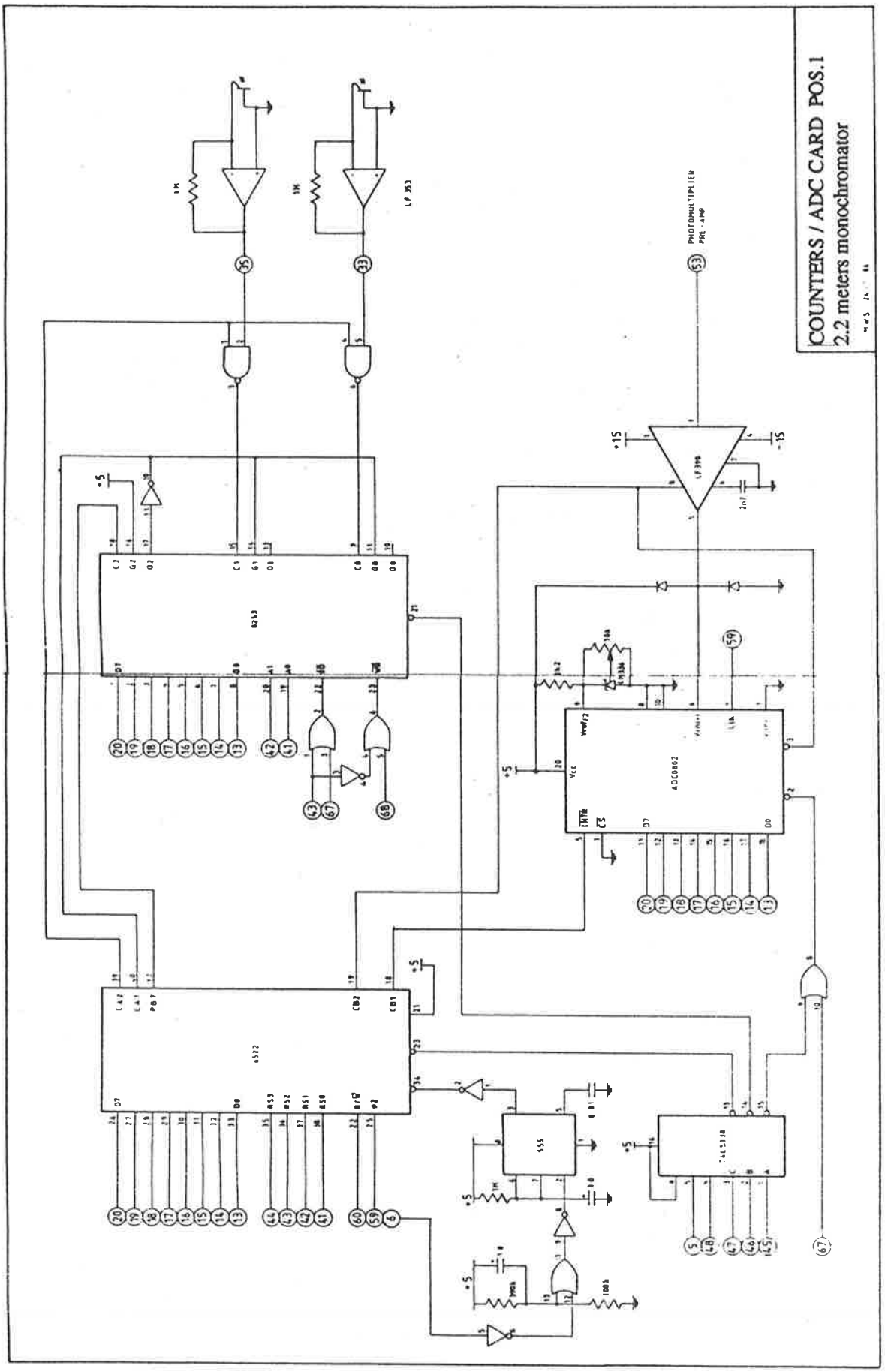

Figure (6-1). Computer interface schematic. Take note that the photomultiplier (53) input to the sample and hold (LF 398) and analogue to digital converter (ADC0802) was not used.

microprocessor bus. The microprocessor reads the data and upon completion of this task initiates the generation of a data taken interrupt signal. The R6522 then commences another count sequence that results in new data being made available to the microprocessor via the above process. The computer program written for the collection of data and a basic explanation of the coding are found in Appendix II.

6.2 Detector linearity

To ensure that the resultant total photoionization cross sections measured are physically relevant it is imperative to show that the entire data sensing and recording apparatus behaves linearly with respect to the input ion currents, or else any non–linearity can be calibrated for, over the whole ion current range. A Keithly Instruments Model 261 Picoammeter providing a 10^{-14} to 10^{-9} A current range was used to test the linearity of the system. A correlation coefficient was measured many times during the experimental period, and was calculated to be better than 0.9995 for both detector circuits over the entire, and all individual decade, ion current ranges.

CHAPTER 7

Data acquisition

7.1 Experimental techniques

In this section I will omit the operational procedures for the commercially available instruments used as this has either already been covered or can be readily gleaned from their respective owner's manuals. I will, however, discuss the practical steps required for the experimental measurement of the total photoionization cross sections.

The vacuum system, encompassing the monochromator and the ion chamber, was pumped by the diffusion pumps for at least 24 hours prior to an experimental run to ensure that the system had reached a pumping speed equilibrium. This also allows out–gassing of the ion chamber to remove any remaining residues from the cleaning processes. As the cross section is dependent on the temperature of the target gas (see section 4.4.2), and the equipment is housed in an air conditioned room, the air conditioner was operated for the same 24 hour period as the pumping system to allow the room and the apparatus to reach an ambient temperature.

The procedure for operation of the lamp has been previously discussed, however, there were problems encountered. The EUV light source when run in the dc mode can be used for cross section measurements almost immediately after ignition as the ion chamber method is insensitive to temporal light fluctuations. However, for use in the pulsed mode, it was crucial to allow approximately 20 minutes for the lamp and/or the spark gap to stabilise to eliminate their interference on other equipment. During this warm–up period the lamp fired erratically and was electromagnetically noisy, interfering with the performance of the pressure transducer and the APC, resulting in the pressure in the ion chamber becoming very erratic. Also the ion current amplifier outputs were driven to rail voltages. The shielding of the lamp and spark gap was increased by cladding 4 mm aluminium sheeting to the outer surfaces of their shields and wrapping the pressure transducer, its cabling and the APC's cabling to the needle valve servo motor with

aluminium foil, but this only resulted in a slight decrease in the magnitude of the fluctuation of the pressure transducer and the ion current amplifiers were still inoperable. The interference was finally suppressed by thoroughly cleaning the lamp's anode and cathode, or their subsequent replacement when badly pitted, the internal and external surfaces of the lamp and the spark gap's electrodes before each experimental run. However, the warm–up period for the lamp was still necessary as the data collected during this period was susceptible to variations. This was demonstrated by connecting a purpose built picoampere source directly onto the ion collector rods and using the computer to measure the currents, firstly with the lamp off and then with the lamp run in the pulsed mode. The picoampere source, consisting of a 1.5 V battery in series with two 10^{11} Ω resistors, was placed inside the brass shield with the detection circuits. With the lamp off, the currents were stable to within $\pm 0.01 \times 10^{-12}$ A (or ±0.05% of the output voltage), however, during the pulsed lamp warm–up period the electrometer's output fluctuated by up to ± 50% for the identical input current. The averaged current amplifier output of twenty data points from each detector circuit with the lamp off was compared to that obtained with the pulsed lamp after the 20 minute warm–up period and was shown to be within ±0.06% with no change in the standard deviation of the measured current. There was virtually no change in the current recorded from when the lamp was run in the dc mode to that with the lamp turned off.

Scattered light entering the ion chamber presented no problems while the lamp was used in the dc mode with a zero "dark" ion current detected when the monochromator was moved off a lamp emission line. However with the lamp used in the pulsed mode the intensity of the scattered light background, as detected by the photomultiplier, increased with decreasing wavelength, initially in a monotonic fashion and then in a parabolic fashion from below ~ 300 Å. The resultant ion currents produced from scattered light entering the ion chamber must be subtracted from the ion currents measured with the monochromator set on an identifiable lamp emission line. This was simply achieved by moving the monochromator off a lamp emission line and measuring the dark ion current. To ensure that only the effect of the scattered light was removed, the monochromator was

moved off–line above and below the emission line where the dark ion currents were found to be similar to within 0.02%. The dark ion currents were then subtracted from the "on–line" ion currents and the resultant "true" ion currents were used in equation (4.7).

The data measured at 584.3 Å by the ion chamber when using the lamp in the dc mode was independently verified using the photomultiplier, by recording the light intensity with firstly no gas and then with gas admitted into the chamber. This assumes that the lamp's intensity remains constant while pumping the gas from the chamber. The worst case produced a match to within approximately 7% with 5% being the best result. Furthermore, wherever possible the cross section data obtained with the lamp operated in one mode is verified using the lamp in the other mode. The only wavelengths for which this was possible was at 583.4 and 303.8 Å. The resultant comparisons were considered to be in excellent agreement, with a relative difference no greater than 1.5% and typically approximately 1.3%.

7.2 Operation of the double ionization chamber

An initial test of the present experimental system was used to corroborate with the findings of Samson and Yin (1989), in particular with the basic variation of the cross section as a function of the gas pressure. A compliance with the form of their curve shape would present a strong credence to their systematic error analysis and give confidence to cross section values measured here at other wavelengths.

Table 7-1 below lists the cross section values measured here for Ar at 583.4 Å and at the listed pressures.

Table 7-1

P(mt)	R	σ_w (Mb)	$\sigma_{w/o}$ (Mb)	σ_E (Mb)
22	1.5	35.43	33.70	34.57
37	1.9	35.51	34.33	34.92
67	3.3	35.87	35.33	35.60
80	4.1	35.85	35.49	35.67
107	6.7	35.93	35.73	35.83
131	10.4	35.90	35.74	35.82
154	15.9	36.05	36.13	36.09
194	33.6	35.96	35.86	35.91

The columns in the above table are, respectively, **P(mt)**- the pressure in the ion chamber in millitorr, **R**- the ratio of the front collector ion current to the back collector ion current, σ_w**(Mb)** and $\sigma_{w/o}$**(Mb)** - the cross sections measured with and without reversal of the electrometers (see Appendix I) in Megabarns ($=10^{-18}$ cm^2), where each cross section value is the mean of ten measurements and σ_E **(Mb)** the experimental cross section, calculated by taking the average of columns 3 and 4. Figure (7-1) is a graph of the cross sections, σ_w**(Mb)** and $\sigma_{w/o}$**(Mb)** from the chart above, as a function of the gas pressure. It is immediately obvious that these curves are comparatively similar to those obtained by Samson and Yin, with due respect for the magnitudes of the systematic errors. The second ion chamber's termination mesh used here is similar to that used by Samson and Yin, therefore the effective reduction in the second ion chamber's length is equal to one mesh hole diameter, that is 1 mm. The maximum fractional error in the ratio (i_1/i_2) was estimated to be ± 1%, and was determined by the maximum rms error of the mean of ion currents detected from the experiment. The reflectance of the terminator was then equated to be approximately 6%, which being almost twice the reflectance of Samson and Yin's could possibly be explained by dehydration of the sodium salicylate coating (Watanabe (1954)), thereby leading to an increase in the reflectance.

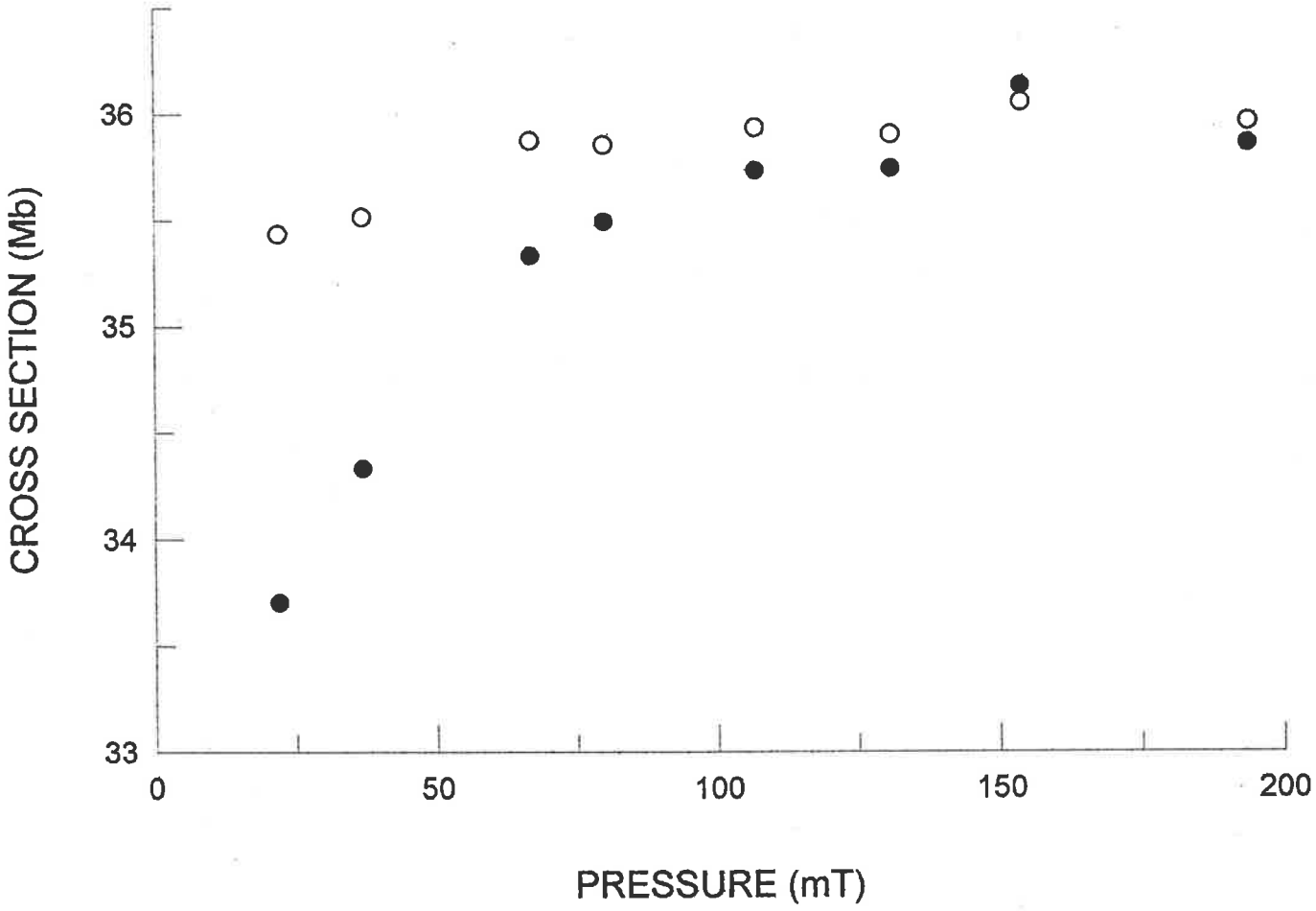

Figure (7-1). Graph of the cross section of Ar measured at 584.3 Å as a function of pressure with (o) and without (o) reversal of the picoammeters.

CHAPTER 8

Experimental Data

8.1 Introduction

Total photoionization cross sections for Ar, O_2 and N_2 are presented here at the He emission lines of 584.3, 537.0, 522.2, 303.8, 256.3, and 243.0 Å. Ar was chosen as the first target gas to be studied because of the inherent simplicity of its photoabsorption mechanism and because of its relatively large photoionization cross sections, thereby providing a performance test for the experimental system.

8.2 Argon total photoionization cross section

Once it was established that the systematic errors for the ion chamber had been correctly accounted for the collection of data could be accurately realised. Table 8–1 below is a compilation of the total photoionization cross section data of argon

Table 8–1

λ (Å)	σ_E (Mb)	R	$\pm S_\sigma$ (Mb)	$\pm \Delta\sigma_R$ (%)	$\Delta\sigma_S$ (%)	$\pm \Delta\sigma_T$ (%)	σ_L (Mb)	$\sigma_L-\sigma_E$ (%)
584.3	35.90	18.7	0.09	1.13	-0.2	1.3	35.98_a	0.2
537.0	35.87	17.9	0.11	1.14	-0.3	1.4	35.25_b	-1.7
522.2	35.10	17.8	0.11	1.12	-0.3	1.4	34.50_b	-1.7
303.8	2.24	1.43	0.12	1.08	-4.6	5.7	2.38_c	5.8

The first column lists the helium emission line wavelengths at which the total photoionization cross sections could be determined using Ar as the target gas. The second column, σ_E **(Mb)**, is a list of the experimental total photoionization cross sections as

calculated here in accordance with the methods explained previously. Column three, **R**, records the averaged ratio of the front to the back ion currents from all measurements. The averaged cross section measurements taken at three pressures, for which R was chosen to reduce the systematic errors associated with the ion chamber and the random errors associated with the uncertainties of the pressure and temperature measurements. For the 303.8 Å data it was necessary to measure the cross section at the maximum allowable pressure in the ion chamber, see below, and also in Appendix I. Column four, lists the standard deviation of the mean cross section value shown in column two. Columns five to seven are, respectively, the random error ($\pm \Delta\sigma_R$ **(%)**), systematic error ($\Delta\sigma_S$ **(%)**), and the resultant total error ($\pm \Delta\sigma_T$ **(%)**) being the greater sum of the systematic and random errors, of the cross section measurements listed in column two. The random error for the experiment was determined using the standard deviation of the data set, because as discussed previously the random error for the pressure measurement could not be accurately determined. The accuracy of the measured cross section will be resolved by comparing the present data with those published by other researchers. The random errors listed in table 8–1 were calculated from the sum of the random errors from each cross section measurement at the one pressure. The random error is dependent upon the preciseness of an experimental measurement and therefore is a record fluctuations in the measurements. The standard deviation is an appropriate measure of the random error of the experiment. Disregarding a lack of precision in the measuring instruments the random error is then calculated from the standard deviation of the observation. The random errors listed in the tables here is the uncertainty associated with the determination of the mean. Nonstatistical fluctuations, which arise from data that exists beyond 3 or 4 standard deviations from the mean were eliminated in accordance to Chauvenet's criterion. This was only necessary for a few data points and was carried out with complete confidence as the data in question always had a large deviation from the mean. The systematic errors were calculated in accordance to the error equations contained in Appendix I. The eighth column, σ_L **(Mb)**, lists the cross sections deemed to be the most accurate as found from a literature survey. Subscripts a, b, c and d refer to the data presented by Samson and Yin

(1989), Marr and West (1976), Samson et al (1991) and Fennelly and Torr (1992) respectively. This nomenclature applies to all the cross sectional data tabled here. The final column, $\sigma_L - \sigma_E$ (%), lists the relative difference between the corresponding cross sections obtained from the literature and those measured here.

The data collected here compares favourably with the data from the literature survey with particular reference to that by Samson and Yin (1989). Their cross section value at 584.3 Å, with an estimated total accumulated error quoted at ±0.8 %, of 35.98 Mb is remarkably close to the cross section measured here of 35.90 Mb. This is to be expected because this work employed an equivalent ion chamber and is methodologically identical to Samson and Yin's, therefore barring any additional sources of errors, the result should be analogous. This would seem to also vindicate the accuracy of the pressure transducer. The cross sectional data collected at 537.0 and 522.2 Å is best compared with the data presented by Marr and West (1976) in which they combined data from their own experiment with those from other workers. The latter data was individually weighted depending upon meeting certain criteria concerning data quality to enhance Marr and West's own data accuracy by, hopefully, reducing the systematic errors associated with all the data used. This was achieved by obtaining a "best" fit value curve by fitting a polynomial to the resultant weighted data points. The total error in the final cross section value was determined from the weighted means, with their own and other worker's data which matched theirs given unity weight, and was calculated using the rms deviation of the polynomial coefficients to be between 2% and 3%. In comparison with my data the cross sections of Marr and West (1976) were both approximately 1.7% low. Since my estimated total error was ± 1.4%, there exists a sufficient overlap of the error margins for the present data to agree with that published by Marr and West. Furthermore the precision of the data presented here is judged to be impressively unimpeachable with a minimal scattering of the individual cross section data values that contribute to the final cross section values. This is supported by a standard deviation of the mean for all groups of twenty data points, taken at the single pressure, at each wavelength being less than 0.3% of the mean cross section value.

Because of limitations due to the length of the ion chamber used here and the maximum permissible target gas pressure the cross section of Ar at 303.8 Å was measured only at the maximum pressure allowable in the ion chamber. Adjusting the 303.8 Å data to allow for the systematic associated with the ion chamber, results in the "improved" cross section value of 2.34 Mb, which lies within the error margin quoted in Samson et al. (1991) of ± 1%. Data for Ar taken at 256.3 and 243.0 Å using the present ion chamber proved to vary widely and be unrepeatable and therefore totally unreliable. Operating the chamber at the highest permissible pressure resulted in a minimal variation of cross section measurements from the mean within the one data collection run of 150%. This is partially due to R being only approximately 1.09 for both wavelengths, which places the cross section values on the steepest section of the appropriate curve, one for each wavelength, similar to figure (7–1). The reduced cross section values effectively results in the translation of the respective curves to higher pressures. Additionally, and more significantly, because of the low cross section value (0.70 and 0.75 Mb respectively, Samson et al., (1991)) and the limitations of the experimental equipment discussed above, the resultant ion currents were of the order of 10^{-12} A. This was only marginally greater than the ion currents produced by the ionizable background radiation present at that wavelength region. The above then combine to produce the large variations in the measured cross sections.

Figure (8–1) is a graph of the total photoionization cross section determined here as a function of the wavelength and superimposed upon those obtained by several other workers, as indicated in the caption beneath the graph.

8.3 Nitrogen total photoionization cross section

Table 8–2 below is a compilation of the cross section data collected here using identical headings to table 8–1

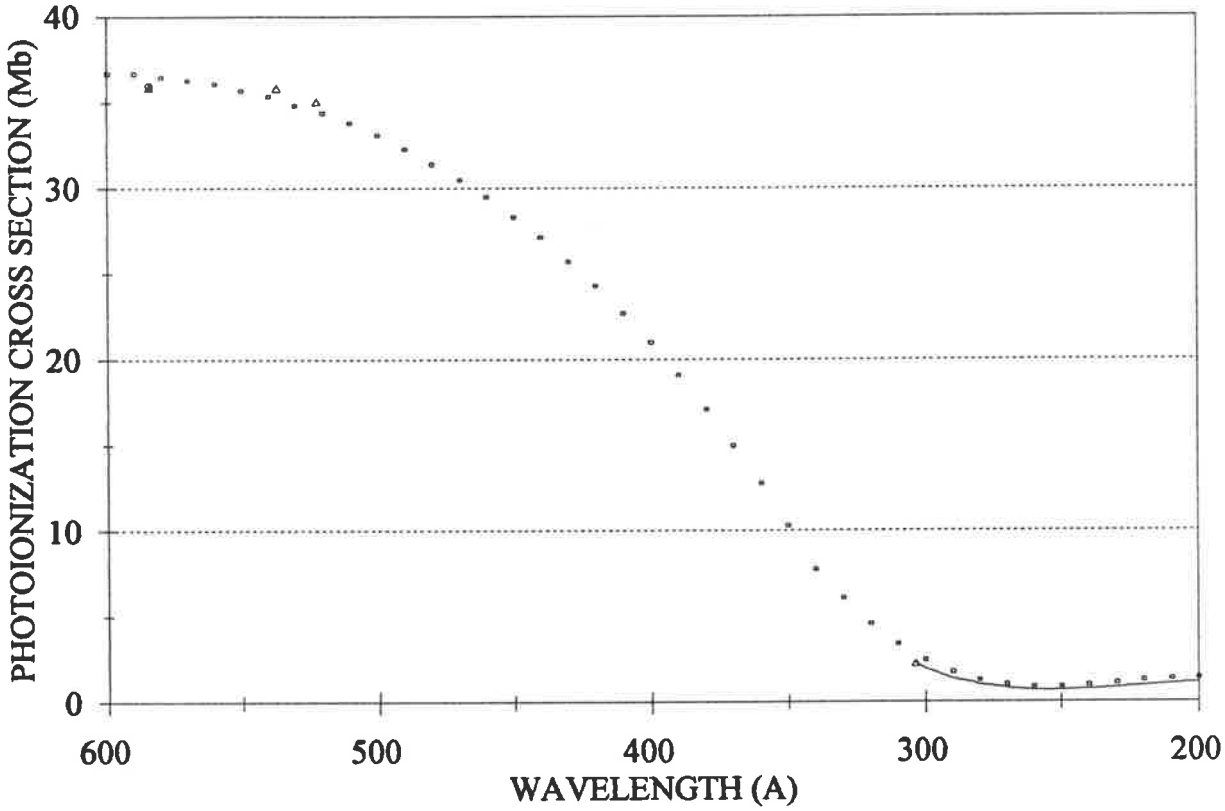

Figure (8-1). Photoionization cross section of argon as a function of wavelength : (Δ) this work ; (□) Marr et al (1976) ; (o) Samson et al (1989) ; (—) Samson et al (1991).

Table 8–2

λ (Å)	σ_E (Mb)	R	$\pm S_\sigma$ (Mb)	$\pm \Delta\sigma_R$ (%)	$\Delta\sigma_S$ (%)	$\pm \Delta\sigma_T$ (%)	σ_L (Mb)	$\sigma_L - \sigma_E$ (%)
584.3	22.77	13.7	0.07	1.04	-0.2	1.3	22.78_a	0.04
537.0	25.75	19.3	0.12	1.03	-0.1	1.2	25.23_d	-2.0
522.2	25.70	19.3	0.09	1.03	-0.1	1.2	24.68_d	-4.0
303.8	11.68	4.0	0.10	1.01	-1.1	2.2	11.70_d	0.2
256.3	10.19	3.4	0.11	1.03	-1.1	2.2	10.21_d	0.2
243.0	9.21	3.1	0.25	1.14	-1.4	2.5	9.68_d	4.8

Figure (8–2) is a graph showing the total photoionization cross section, as determined here, as a function of the wavelength and superimposed upon the data from other researchers as indicated in the caption beneath the graph. Similarly with the cross section of Ar, the cross section for N_2 at 584.3 Å measured here has a relative difference with Samson and Yin's of just 0.04%. The cross sections measured at 537.0 and 522.2 Å are both greater than that quoted by Fennelly and Torr (1992). Their data was a compilation of experimental and theoretical cross sections using the most recent measurements where discrepancies existed between sets of data. However the error margins of the data presented here overlaps with those quoted by Fennelly and Torr. Adjusting the 303.8, 256.3 and 243.0 Å data to allow for the systematic associated with the ion chamber, results in the "improved" cross section values of 11.81, 10.30 and 9.34 Mb. These differ from that contained in Fennelly and Torr (1992) by –0.9%, –0.9% and +3.5%. The overlap of the error margins of the present data and that of Fennelly and Torr (± 3%) for the data taken at 303.8 and 256.3 Å is very good. The 243.0 Å data, though there exists a large relative error with Fennelly and Torr's data, still presents an overlap of their error margins.

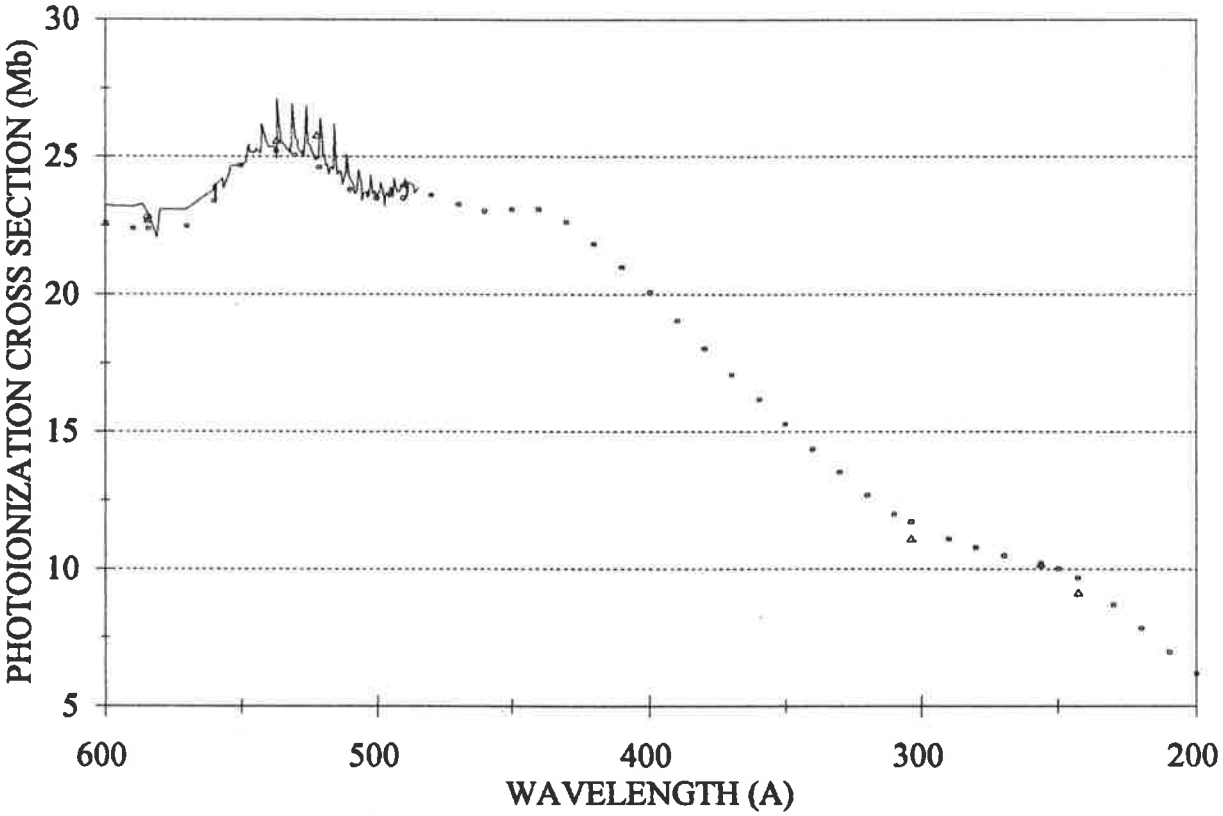

Figure (8-2). Photoionization cross section of nitrogen as a function of wavelength : (Δ) this work ; (□) Fennelly et al (1992) ; (o) Samson et al (1989) ; (—) Holland et al (1993).

8.4 Oxygen total photoionization cross section

Table 8–3 below is a compilation of the total photoionization cross section data collected for this work using identical headings to table 8–1.

Table 8–3

λ (Å)	σ_E (Mb)	R	$\pm S_\sigma$ (Mb)	$\pm \Delta\sigma_R$ (%)	$\Delta\sigma_S$ (%)	$\pm \Delta\sigma_T$ (%)	σ_L (Mb)	$\sigma_L - \sigma_E$ (%)
584.3	22.87	13.6	0.07	1.04	-0.2	1.3	22.95_a	0.3
537.0	26.48	23.7	0.08	1.07	-0.1	1.2	25.25_d	-4.8
522.2	24.40	16.5	0.08	1.05	-0.2	1.3	24.58_d	0.7
303.8	15.97	7.1	0.10	1.01	-0.2	1.2	16.81_d	5.0
256.3	13.54	5.5	0.17	1.02	-0.6	1.6	13.37_d	-1.3
243.0	12.37	4.7	0.18	1.13	-0.8	1.9	12.17_d	-1.6

Figure (8–3) is a graph showing the total photoionization cross section, as determined here, as a function of the wavelength and superimposed upon the data from other researches as indicated in the caption below the graph.

The present data for 584.3 Å is again similar to Samson and Yin's (1989) for the reasons discussed above. The remaining He I data is inconsistent with that quoted in Fennelly and Torr with the present 537.0 Å cross section value at a large -4.8% variance, whereas the present 522.2 Å cross section value differs by only 0.7% from Fennelly and Torr. However for the 537.0 Å present cross section and that of Fennelly and Torr the error margins just overlap. Once again an adjustment of the present data can be made to allow for the systematic errors associated with the ion chamber used for the cross sections measured at 303.8, 256.3 and 243.0 Å, resulting in "improved" cross section values of 16.00, 13.62 and 12.47 Mb respectively. These differ from that contained in Fennelly and Torr (1992) by +4.8%, –1.9% and –2.5%. The 303.8 Å cross section value was verified to

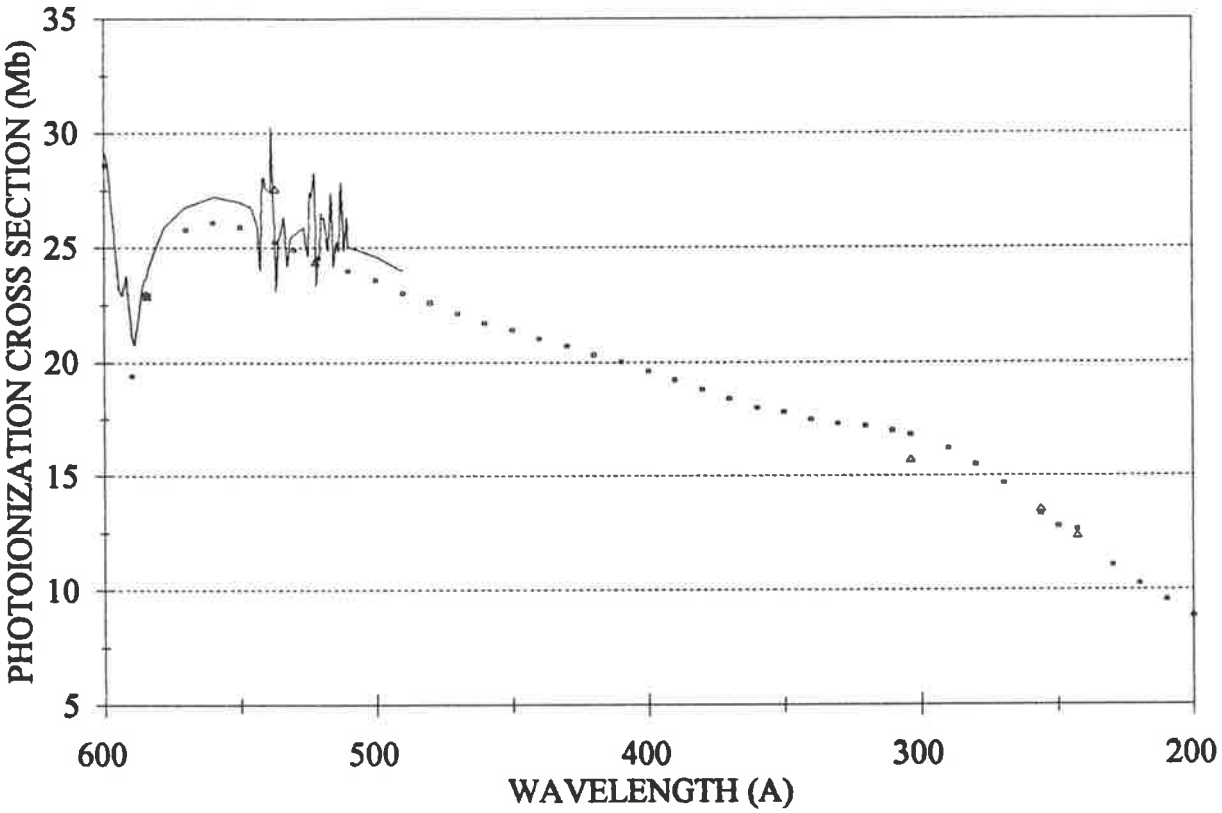

Figure (8-3). Photoionization cross section of oxygen as a function of wavelength : (Δ) this work ; (□) Fennelly et al (1992) ; (o) Samson et al (1989) ; (—) Holland et al (1993).

1.4% (16.23 Mb) with the lamp operated in the dc mode. The He II data nevertheless exhibits good agreement to that of Fennelly and Torr.

APPENDIX I

SYSTEMATIC ERRORS OF THE EXPERIMENTAL DOUBLE ION CHAMBER

The principle aim of this appendix is to examine the systematic errors associated with the specific design of the ion chamber used here. This has already been performed by Samson and Yin (1989), so I will here present a synopsis of their findings.

This will entail a discussion of (1) the absolute accuracy of the electrometers used to determine i_1 and i_2 and (2) the method used to terminate the second ion chamber and it's effect upon the resultant values of i_1 and particularly i_2.

(1) The electrometers have been fully described in Chapter 4. Both displayed a high degree of linearity during the experimental period, with the smallest correlation coefficient calculated at 0.9995. The outputs from both electrometers with a constant input current increased at a maximum of 5% per hour, because of internal heating of the electrometer chip, with an average of 3.6% per hour. However tests showed that the linearity of both electrometers were not unduly effected for periods lasting up to two hours which was approximately triple the maximum length of time of any experimental run. However it is crucial to determine the consequence of an error in the absolute accuracy of both or either of the electrometers used to measure i_1 and i_2 on the cross section measurement and if required to ascertain a solution. The ideal cross section is given by

$$\sigma = \left(\frac{1}{n L}\right) \ln\left(\frac{i_1}{i_2}\right) \qquad \text{(A1.1)}$$

However, with a fractional error f in the ratio (i_1 / i_2), the actual measured cross section is given by

$$\sigma' = \left(\frac{1}{n L}\right) \ln\left(\frac{i_1}{i_2}\right) (1 \pm f) \qquad \text{(A1.2)}$$

The fractional error biases the measured cross section either positive or negative from the true value, depending upon which electrometer is used to measure i_1 or i_2. However the magnitude of the fractional error is a constant. Combining equations A1.1 with A1.2 leads to the relative error in the cross section measurement being given by

$$\frac{(\sigma' - \sigma)}{\sigma} = \left(\frac{1}{\sigma n L}\right) \ln(1 \pm f) \qquad \text{(A1.3)}$$

Then the relative error in σ decreases, for a constant value of f, with an increase in the number density, or the pressure. The error due to a fractional error in the ratio (i_1/ i_2) can then be eliminated by making a measurement of the cross section at a sufficiently high pressure, or alternatively by making a measurement of the cross section and then reverse the inputs to the electrometers, repeating the measurement, and taking an average of the two measurements. To eliminate any further calibration errors the electrometers were always used with their concurrent circuitry. Figure (A1–1) is a graph depicting the cross section that is measured for a ± 1% error in the ratio (i_1/ i_2) as a function of the pressure with the curves labelled ± b.

(2) Another systematic error associated with the present experimental ion chamber arises from the method used to terminate the second ion chamber.

A detector such as a photomultiplier is mandatory when using a line source to locate the wavelength at which the cross section is to be measured. To terminate the second ion chamber and allow the monitoring of the incident radiation a 90% transparent mesh was used. A plastic light pipe coated with sodium salicylate was placed behind and in contact with the mesh. The photomultiplier was then bolted onto a flange that is connected to the ion chamber's vacuum chamber which bought it into contact with the

back face of the light pipe. This arrangement had been shown (Samson and Yin (1989)) to have a minimum impact on reducing the ion current magnitudes. From this set–up the systematic errors in the method of terminating the present ion chamber are (i) reflection from the terminator and (ii) the reduction in the effective length of the second chamber.

(i) Using the same nomenclature as in section 4.3 the intensity of the incident radiation into the ion chamber is given as I_0. Then the number of ions formed above each collector during the initial passage of light beam is given by

$$\frac{i_1}{e} = \gamma I_0 \left[1 - \exp\left(-\sigma n L\right)\right],$$

$$\frac{i_2}{e} = \gamma I_0 \left[1 - \exp\left(-\sigma n L\right)\right] \exp\left(-\sigma n L\right) \qquad \text{(A1.4)}$$

where γ is the ionization efficiency of the gas at that wavelength. Upon reflection of the light beam, additional number of ions formed above each collector electrode need to be included into equation (A1.4), but with the term ($r I_0 \exp(-\sigma n L)$) substituted for I_0, where r is the reflectance of the terminator. However, the last exponential term from the second equation in (A1.4) is now appended to the equation calculating the current from the first chamber, which upon reflection from the ion chamber is now treated as the second chamber. Then after combining the two sets of equations for the front and back ion chambers to produce the total number of ions formed above each electrode and taking the logarithm of the ratio of the two resultant equations produces the relative error in the cross section which is given by

$$\left(\frac{\sigma' - \sigma}{\sigma}\right) = \left(\frac{1}{\sigma n L}\right) \ln\left[\frac{1 + r \exp\left(-3 \sigma n L\right)}{1 + r \exp\left(-\sigma n L\right)}\right] \qquad \text{(A1.5)}$$

and is plotted in figure (A1–1) as a function of the pressure for a reflectivity of 5% and with the curve labelled c.

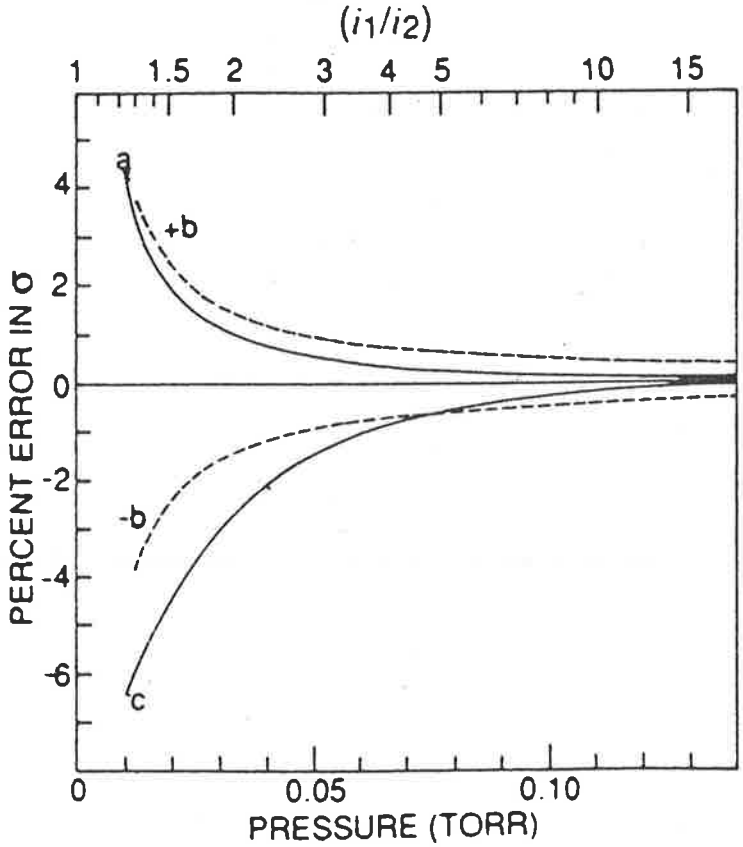

Figure (A1-1). Percent error in the photoionization cross section as a function of gas pressure for the following systematic errors that are associated with the present ion chamber design: ±1% error in the ratio (i_1 /i_2), dashed curves marked ±b; error caused by a 5% reflectance from the rear terminator, solid curve marked c; error caused by a 1% effective reduction in the length of the second ion collector electrode caused by ions lost to the terminator, solid curve marked a (Samson and Yin (1989).

(ii) The light pipe is an insulator and due to photoemission will begin to accumulate a positive charge. An intense electric field between the pipe and the terminator mesh results that will penetrate the mesh's holes into the chamber and attract ions formed in the chamber to the pipe. As the number of ions collected by the insulator increases, and no other processes were to intervene, then the charge on the insulator would increase until it reached the mesh's potential and the loss of ions from the ion chamber would halt. However photoelectrons formed within the chamber are accelerated towards the mesh and if the field between the mesh and the insulator was sufficiently reduced the photoelectrons will reach the insulator hence increasing the field strength. Therefore an equilibrium is reached where the number of ions and photoelectrons onto the insulator is constant. The ions lost to the pipe originate approximately one hole diameter into the chamber from the mesh Samson and Yin (1989)). Then the net effect is a reduction of the effective length of the second ion electrode. The mesh used has hole diameters of approximately 1 mm, so the net result is a decrease of L for the second chamber of 1 mm. The number of ions produced above each collector is then given as

$$\frac{i_1}{e} = \gamma I_0 \left[1 - \exp\left(-\sigma n L\right)\right],$$

$$\frac{i_2}{e} = \gamma I_0 \exp\left(-\sigma n L\right)\left[1 - \exp\left(-\sigma n L'\right)\right] \qquad \text{(A1.6)}$$

and once again, taking the logarithm of the ratio of (A1.6) results in the relative error of the cross section and is given by

$$\left(\frac{\sigma' - \sigma}{\sigma}\right) = \left(\frac{1}{\sigma n L}\right) \ln\left[\frac{1 - \exp\left(-\sigma n L\right)}{1 - \exp\left(-\sigma n L'\right)}\right] \qquad \text{(A1.7)}$$

which is plotted in figure (A1–1), with a reduction of L by 1% (L' = 0.99L), as a function of the pressure and as the solid curve marked a.

APPENDIX II

CBM–INTERFACE PROGRAM

```
100     BASIC ROUTINE TO SET–UP 6522 AND 8253 REGISTERS
110     FOR THE 2.2 M MONOCHROMATOR
200     DATA 169, 195, 141, 37, 137, 169, 238, 141, 44, 137, 96
210     FOR I = 634 TO 644
220     READ A; POKE I, A
230     NEXT I
1000    C1 = 35086
1010    V1 = 35102
1103    INPUT "HOW MANY DATA POINTS" ;K
1105    DIM X(K), Y(K), Z(K)
1106    FOR J = 1 TO K : GOTO 1110
1110    POKE V1 +2, 128 : POKE V1 + 4, 80
1120    POKE V1 + 11, 192 : POKE V1 + 12, 236
1130    POKE V1 +14, 0
1200    POKE C1 +7, 48 : POKE C1 + 4, 255 : POKE C1 + 4, 255
1210    POKE C1 + 7, 112 : POKE C1 + 5, 255 : POKE C1 + 5, 255
1220    POKE C1 + 7, 176 : POKE C1 + 6, 9 : POKE C1 + 6, 0
2050    LET X (J) = ((255 - PEEK (C1)) + (256 * (255 - PEEK (C1))))
2060    PRINT J
2070    PRINT X(J) "Hz" ,,
2080    LET Y (J) = ((255 - PEEK (C1 + 1)) + (256 *(255 - PEEK (C1 + 1))))
2090    PRINT Y(J) "Hz" ,,
3035    IF E$ = "Y" THEN PRINT #2, X (J); CHR$ (13);Y (J)
3045    FOR I = 1 TO 1000 : NEXT I
3050    NEXT J
4000    END
```

CBM PROGRAM GUIDE

The addresses for the interface board are –

C1 = 35088 = Chip select for the 8253 counter
V1 = 35120 = Chip select for the SY6522 controller chip

6522

Line 200 initiates the PB7 pulses and enables count inputs. The PB7 pulse is used to provide gating for the data pulses into the programmable interval timer. It is written in machine language to facilitate the initiation of the processes required to enable data from the ion chamber, in the form of pulses, to be placed onto the microprocessor's bus.

POKE V1 + 2, 128 Data direction register B programmed an output. Timed interrupt each time the interrupt timer, "T1", is loaded resulting in a single programmable width pulse or a one-shot output.

POKE V1 + 4, 80 T1 low-order counter. T1 programmed to produce a single negative pulse on the PB7 peripheral pin.

POKE V1 + 11, 192 Address the Auxiliary control register. T1 produces a square-wave output.

POKE V1 + 12, 236 Address the Peripheral control register. CB2 is set high and CB1 set low for write handshaking of the PB port with the peripheral device on CA1 and CA2 with both set for an interrupt control with a negative active edge. This basically disables the 8253 and enables the A/D converter, (not used, see chapter 6), for the recording of the pressure in the double ionization chamber if the data run is to be saved onto floppy disk for latter analysis.

POKE V1 + 14, 0 Bit 7 of the interrupt enable register is loaded with a 0 thereby setting and clearing all the interrupt flag registers.

8253

POKE C1 + 7, 48
POKE C1 + 7, 112
POKE C1 + 7, 176 Mode 0 loaded to the 0, 1, 2 counters respectively.

POKE C1 + 4, 255 : POKE C1 + 4, 255
POKE C1 + 5, 255 : POKE C1 + 5, 255

Counters 1 and 2 loaded with the maximum count (65,535) which is loaded LSB first. Counters are now ready to perform their duties.

POKE C1 + 6, 9 : POKE C1 + 6, 0

Counter 0 is loaded, (LSB first), with the number of P7 clock pulses, with the P7 clock pulses set at 0.13 s, then the period for which the counter window is open is set to 1.17 s.

BIBLIOGRAPHY

Allen, K. R., Phillip, K., (1964) Proc. Roy. Soc. Ser. A., 278 , 188

Analogue Devices Data Manual, (1976)

Anders, A., Anders, S., Gundersen, M. A.,(1993), Phys. Rev. Lett. 71 , #3, 364

Babich, L. P., Stankevich, Y. L., (1973), Sov. Phys.–Tech. Phys. 17 , 1333

Banwell, C. N., (1972), Fundamentals of Molecular Spectroscopy (McGraw–Hill)

Bennett, W. H., (1934), Phys. Rev., 45 , 890

Berkowitz, J., (1979), Photoabsorption, Photoionization and Photoelectron Spectroscopy, (Academic)

Bethe, H. A., Salpeter, E. E., (1957), Quantum Mech. of One–and Two–Electron Atoms (Springer–Verlag)

Blackwell, H.E., Shipp, G.S., Ogawa, M., Weissler, G.L., 56 #5, 665 (1966)

Bloess, D. et al, (1983), Nuclear Instr. and Methods, 205, 173

Boenig, H. V., (1982), Plasma Science & Technology, (Cornel Univ. Press)

Carr, W.R., (1903), Phil. Trans. Roy. Soc. London, A201 , 403

Clayton, G., Newby, B., (1992), Operational Amplifiers, (Newnes, Oxford)

Cobine, S. D., (1958), Gaseous Conductors, (Dover Publications)

Cohen, H. D., Fano, U., (1966), The Phys. Rev., 150 , #1, 30

Cole, B. E., Dexter, R. N., (1977), J. Phys. B: Atom. Molec. Phys. 11 , #6, 1011

Cook, G. R., Metzger, P. H., (1964), The J. of Chem Phys., 41 , #2, 321

Cooper, J. W., (1962), The Phys. Rev., 128 , #2, 681

Dehmer, A. A., Dill, D., Wallace, S., (1979), Phys. Rev., Lett., 43 , 1005

Doran, A. A., (1968), Z. Phys., 208 , 427

Fennelly, J. A., Torr, D. G., (1992), Atomic Data and Nuclear Data Tables, 51 , 321

Fisher, L. H., Bederson, B., (1951), Phys. Rev. 81 , 109

Fock, V., (1930), Z. Physik. 61 , 126

Gascoigne, J., (1971), Vacuum 21 #'s 1/2, 21

GCA/McPherson Instrument Manual, (1968)

Gewartowski, J. W., Watson, H. A., (1965), Principles of Electron Tubes, (Van Nostrand)

Gilmore, F. R., (1965), J. Quant. Spec. Rad. Transf. 5, 369

Guntherschulze, A., (1930), Z. Tech. Phys., 11 , 49

Hartree, D. R., (1928), Proc. Cambridge Phil. Soc., 24 , 111

Hertzberg, G. (1950) Molecular Spectra and Molecular Structure I. Spectra of Diatomic Molecules, (Van Nostrand Reinhold Company)

Holland D. M. P., Shaw D. A., McSweeney S. M., McDonald M. A., Hopkirk A., Hayes M. A., (1993), Chemical Physics, 173 , 315

Hudson, R. D., Carter, V. L., (1968), J. Opt. Soc. of Am., 58 , #2, 227

Intersil Data Manual, (1982)

Kerridge, B., (1991), EDN, #6

Kunhardt, E. E., Byszewski, W. W., (1980) Phys. Rev. A, 21 , 2069

Llewellyn Jones, F., Henderson, A., Arch. Electrotech., 28 , 185, (1939)

Llewellyn Jones, F., (1966), Ionization and Breakdown in Gases. (Methuen)

Loeb, L. B. (1939), Fundamental Processes of Electrical Discharges in Gases. (Wiley)

Lohmann, B and Weigold E (1981) Physics Letters 86A #3 p 139

Marr, G. V. (1968) Plasma Spectroscopy, (Elsevier)

Marr, G. V., West, J. B., (1976), Atom. Data and Nucl. Data Tables, 18 , #5, 498

Mason, J. H.,(1978), IEEE Trans. Electr. Insul. EI-13 , #4, 211

Meek, J. M., (1940), Phys. Rev. 57 , 722

Mesyats, G. A., Bychdov, Y. I., Kremmer, V. V., (1972), Sov. Phys.–Usp., 15 , 282

Milne, E. A., (1924), Phil. Mag., 47, 209

Nasser, E., (1971), Fundamentals of Gaseous Ionization and Plasma Electronics, (Wiley–Interscience)

Newberg, R. G., Heroux, L., Hinteregger, H.E., Applied Optics, 1 #6, 733 (1962)

Ngo, M. T., Schoenbach, K. H., Gerdin, G. A., Lee, J. H., (1990), IEEE Trans. on Plasma Science, 18 , #3, 669

Pak, H., Kushner, M. J., (1989), J. Appl. Phys. 66 , 2325

Paresce, F., Kumar, S., Bowyer, C. S., Applied Optics, 10 #8, 1904 (1971)

Paschen, F., (1889), Wied. Am. 37 69

Paschen, F., (1916), Ann. Phys 50 , 901

Raether, H., (1939), Z. Phys. 112 , 464

Reid, H. J., (1977), AERE - R 8577, UKAEA Harwell

Rogowski, W., Tamm, R., (1928), Arch. Elektrotek., 20 , #107, 625

Samson, J. A. R., (1964a), J. of the Optical soc. of America, 54 , #1, 6

Samson, J. A. R., (1964b), J. of the Optical Soc. of America, 54 , #7, 876

Samson, J. A. R., (1967), Techniques of Vacuum Ultraviolet Spectroscopy, (Wiley)

Samson, J. A. R., Gardner, J. L., Haddad, G., N., (1977),J. of Electron Spectroscopy and Related Phenomena, 12 , 281

Samson, J. A. R., (1980), U.S. Patent # 4,199,703

Samson, J. A. R., Masuoka, T., Pareek, P. N., Angel, G. C., (1987), J. Chem. Phys. 86 , #11, 6128

Samson, J.A.R., Yin, L., (1989), J. Opt. Soc. Am. B. 6 , 2326

Samson, J.A.R., Lyn, L., Haddad, G. N., Angel, G. C., (1991), J. De Phys IV, 1 , C1–99

Seaton, M. J., (1951), Proc. Roy. Soc. Lond., Ser. A 208 , 418

Sommerfield, A., (1930), Wave Mechanics, (Methuen & Company)

Starnevich, Y. L., Kalinin, V. G., (1968), Sov. Phys.–Dokl., 12 , 1042

Tarasova, Y. L., Khundyakova, L. N., Loiko, T. V., Tsukerman, V. A., (1974), Sov. Phys.–Tech. Phys., 19 , 351

Townsend, J. S., (1910), The theory of ionization of gases by collisions (Constable)

Von Engel, A., (1983), Electric Plasma's: Their Nature and Uses, (Taylor & Francis)

Wainfan, N., Walker, W. C., Weissler, G. L., (1953), J. Appl. Phys., 24 , #10, 1318

Ward, A. L., (1965), Phys. Rev., 180 , A1357

Watanabe, K., (1954), J. Chem. Phys., 22 , #9, 1564

West, J. B., Marr, G. V., (1976), Proc. Roy. Soc. Lond. A 349 , 397

Yu, Z., Rocca, J., Meyer, J., Collins, G., (1982), J. Appl. Phys., 53 , #7, 4704

Zsanszky, K., (1973), Nuclear Instruments and Methods, 112 , 299